nature nanotechnology

ARTICLES

PUBLISHED ONLINE: 21 MARCH 2016 | DOI: 10.1038/NNANO.2016.38

A graphene-based electrochemical device with thermoresponsive microneedles for diabetes monitoring and therapy

Hyunjae Lee[1,2†], Tae Kyu Choi[1,2†], Young Bum Lee[1,2†], Hye Rim Cho[1,3], Roozbeh Ghaffari[4], Liu Wang[5], Hyung Jin Choi[6], Taek Dong Chung[7,8], Nanshu Lu[5], Taeghwan Hyeon[1,2], Seung Hong Choi[1,3] and Dae-Hyeong Kim[1,2*]

Owing to its high carrier mobility, conductivity, flexibility and optical transparency, graphene is a versatile material in micro- and macroelectronics. However, the low density of electrochemically active defects in graphene synthesized by chemical vapour deposition limits its application in biosensing. Here, we show that graphene doped with gold and combined with a gold mesh has improved electrochemical activity over bare graphene, sufficient to form a wearable patch for sweat-based diabetes monitoring and feedback therapy. The stretchable device features a serpentine bilayer of gold mesh and gold-doped graphene that forms an efficient electrochemical interface for the stable transfer of electrical signals. The patch consists of a heater, temperature, humidity, glucose and pH sensors and polymeric microneedles that can be thermally activated to deliver drugs transcutaneously. We show that the patch can be thermally actuated to deliver Metformin and reduce blood glucose levels in diabetic mice.

High-quality, large-area graphene, synthesized by a chemical vapour deposition (CVD) process[1,2], constitutes an extremely useful material for emerging transparent and deformable electronics. Graphene exhibits outstanding mechanical[3], electrical[4] and optical properties[5], by virtue of its soft carbon-based nature[6], high carrier mobility[7] and ultrathin form factor. The large-scale processibility[1,2] and biocompatibility[8] of graphene further facilitate its numerous consumer and healthcare applications. However, the low defect density of CVD graphene compared with reduced graphene oxides[9,10] results in poor electrochemical activity. Defect sites have high electrochemical activity and are useful for various electrochemical sensors[8]. Although high-quality CVD graphene has advantages in large-area arrayed configurations[11,12], it has limited uses in electrochemical devices for the detection of biochemical markers such as pH[13], ions[14] and biomolecules[15,16].

Meanwhile, the continuous point-of-care monitoring of biomarkers based on electrochemical sensing, together with real-time physical sensing and actuation[17–20], provide unique solutions for the treatment of chronic, homeostasis-related diseases such as diabetes mellitus. There is a significant need for noninvasive monitoring of important markers of such diseases using multifunctional portable/wearable device arrays[21,22]. A feedback therapeutic system that completes the loop of sensing and therapy[21] could significantly improve the quality of care management. Here, we report the development of skin-mounted graphene-hybrid (GP-hybrid) device arrays capable of not only sweat-based glucose and pH monitoring in conjunction with a sweat-control layer, but also controlled transcutaneous drug delivery through bioresorbable temperature-responsive microneedles. Precise measurements of sweat glucose concentrations can be used to estimate the levels of glucose in the blood based on previously reported correlations[23–25]. Moreover, integrated sensors for tremor detection under hypoglycaemic conditions and skin temperature monitoring during thermal actuations induced by drug delivery could further help prevent the overdose of drugs and low-temperature burns, respectively. Finally, the connection of GP-hybrid wearable devices to a portable/wireless power supply and data transmission unit would enable the point-of-care treatment of diabetes.

Device design and material strategy for the diabetes patch

The integrated system consists of the following modules: sweat-control components (a sweat-uptake layer and waterproof film), sensing components (humidity, glucose, pH and tremor sensors) and therapeutic components (microneedles, a heater, and a temperature sensor), as shown in Fig. 1a,b. The bilayer of a Au serpentine mesh and gold-doped CVD graphene (Fig. 1c, bottom) ensures high conductivity, mechanical reliability and optical transparency for stable electrical signal transfer as well as a semi-transparent skin-like appearance in the large-area deformable device array configuration. The selective, patterned functionalization of the gold-doped CVD graphene with electrochemically active, soft materials (Fig. 1a,b, left and Fig. 1c, top) establishes GP-hybrid sensors with enhanced electrochemical activity and biochemical sensitivity/selectivity, while maintaining the intrinsic softness of graphene. In contrast to conventional liquid-type bulky counter electrodes used for electrochemical sensing, solid-state Ag/AgCl counter electrodes

---

[1]Center for Nanoparticle Research, Institute for Basic Science (IBS), Seoul 151-742, Republic of Korea. [2]School of Chemical and Biological Engineering, Institute of Chemical Processes, Seoul National University, Seoul 151-742, Republic of Korea. [3]Department of Radiology, Seoul National University College of Medicine, Seoul 110-744, Republic of Korea. [4]MC10, 10 Maguire Rd., Lexington, Massachusetts 02140, USA. [5]Center for Mechanics of Solids, Structures and Materials, Department of Aerospace Engineering and Engineering Mechanics, Texas Materials Institute, University of Texas at Austin, 210 E 24th Street, Austin, Texas 78712, USA. [6]Department of Anatomy, Neuroscience Research Institute, Seoul National University College of Medicine, Seoul 110-744, Republic of Korea. [7]Department of Chemistry, Seoul National University, Seoul 151-747, Republic of Korea. [8]Advanced Institutes of Convergence Technology, Gyeonggi-do 443-270, Republic of Korea. †These authors contributed equally to this work. *e-mail: dkim98@snu.ac.kr

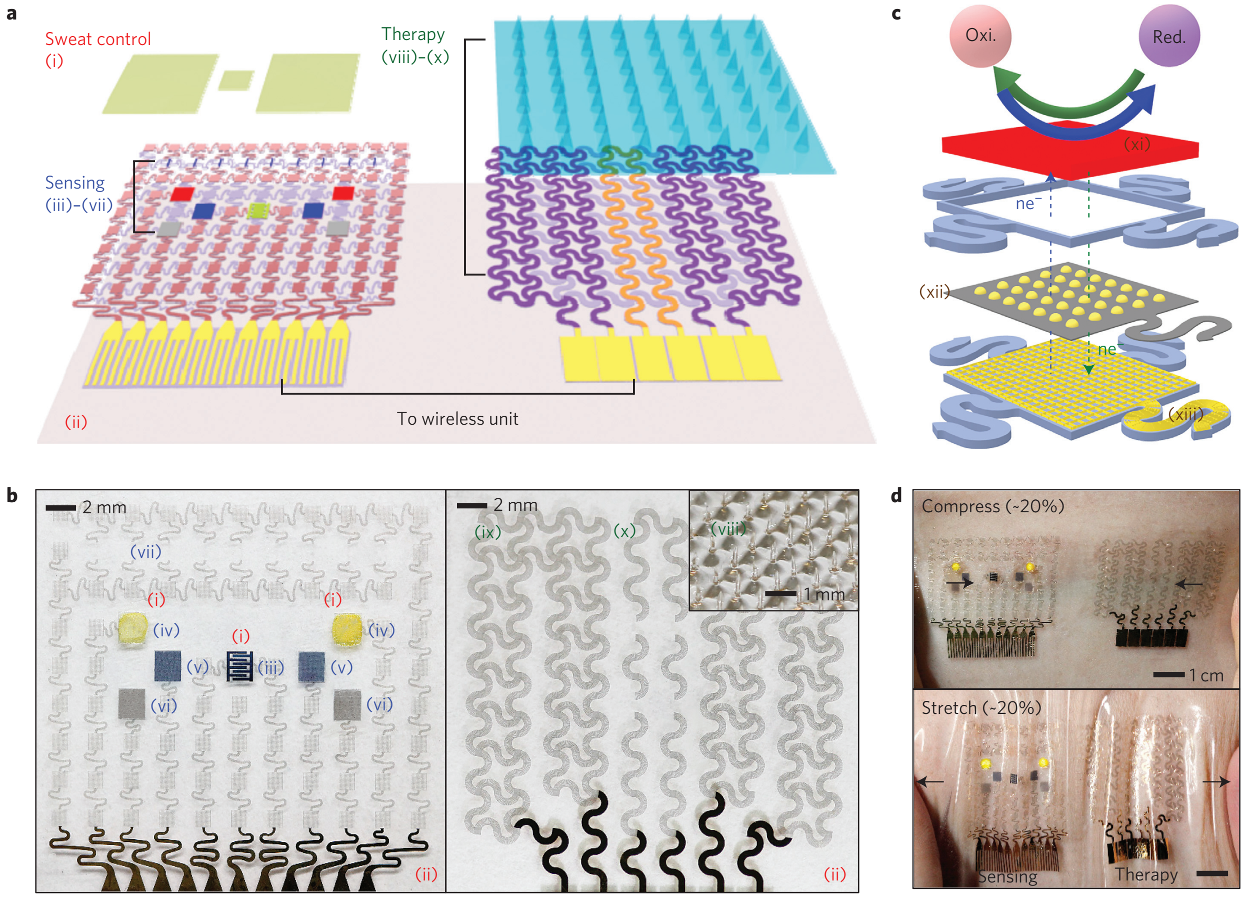

Figure 1 | Schematic drawings and corresponding images of the GP-hybrid electrochemical devices and thermoresponsive drug delivery microneedles. **a**, Schematic drawings of the diabetes patch, which is composed of the sweat-control (i, ii), sensing (iii–vii) and therapy (viii–x) components. **b**, Optical camera image of the electrochemical sensor array (left), therapeutic array (right) and magnified view of the drug-loaded microneedles (inset). (i) sweat-uptake layer (Nafion); (ii) water-proof film (silicone); (iii) humidity sensor (PEDOT); (iv) glucose sensor (PB); (v) pH sensor (PANi); (vi) counter electrode (Ag/AgCl); (vii) tremor sensor (graphene); (viii) microneedles with drugs (PVP@PCM); (ix) heater (Au mesh/graphene); (x) temperature sensor (graphene). **c**, Schematic of the GP-hybrid electrochemical unit, which consists of electrochemically active and soft functional materials (xi), gold-doped graphene (xii) and a serpentine Au mesh (xiii), from top to bottom. **d**, Optical camera images of the diabetes patch laminated on human skin under mechanical deformations.

(included in the sensor components; Fig. 1a,b) provide portability and wearability of the electrochemical system. Bioresorbable polymer-based microneedles[26,27] coated with the phase-change material (PCM)[28] release the drug into the bloodstream when the the programmed threshold temperature is exceeded (Fig. 1a, right and Fig. 1b, inset). Multichannel thermal actuators (Fig. 1b, right) control the amount/rate of drug release in a stepwise manner. Soft materials with stretchable designs provide extremely conformal contacts to the human skin under deformation (Fig. 1d). This conformal and intimate interfacing enables stable sensing and efficient drug delivery. If the patch is delaminated, sensing and drug delivery are not effective. More details of the system integration and combined operations including portable/wireless units and sweat-control layers are described in Supplementary Figs 1–3.

Characterization of the GP-hybrid

The electrochemical properties of the GP-hybrid are characterized and compared with controls (an Au film and Au mesh). Optical (left) and scanning electron microscope (SEM; right) images of the individual electrodes with the poly(3,4-ethylenedioxythiophene) (PEDOT) functionalization by the galvanostatic electrodeposition are shown in Fig. 2a. Large-scale views are included in Supplementary Fig. 4. The amount of functional materials deposited on the Au mesh (Fig. 2a, middle) is much less than that on the Au film (Fig. 2a, top) or GP-hybrid (Fig. 2a, bottom) electrodes because of the non-conducting square regions of the mesh. Au particles on doped graphene form scattered clusters of functional materials on the GP-hybrid surface. The GP-hybrid, therefore, exhibits better electrochemical performance characteristics due to its large electrochemically active surface area under bare electrode conditions (Fig. 2b–d) as well as during (Fig. 2e–g) and after (Fig. 2h–j) the functionalization.

Cyclic voltammograms (CV; Fig. 2b and Supplementary Fig. 5a) and alternative current (a.c.) impedance measurements (Nyquist plots in Fig. 2c and Supplementary Fig. 5b, Bode plots in Fig. 2d) for $Fe(CN)_6^{3-/4-}$ redox coupling demonstrate the higher charge storage capacity (CSC) and lower interfacial impedance of the electrode of the GP-hybrid than controls (see Supplementary Section 1.1 for details). The Au mesh shows the highest charge transfer resistance (R_{ct}) and its CV peak shifts to higher potentials due to the small active area and low electrochemical activity. The electrode of the GP-hybrid, bilayer of gold-doped CVD graphene and Au mesh, however, compensates for the non-conducting regions of the Au mesh by doped graphene, which enlarges the electrochemically active surface area to slightly larger than that of the Au film. The estimated electrochemically active surface areas of these electrodes are summarized in Supplementary Table 1. Related discussions are described in Supplementary Section 1.1. The electrochemical stability/reliability of the GP-hybrid electrode is further proven through temperature-dependent impedance measurements and multiple CV operations

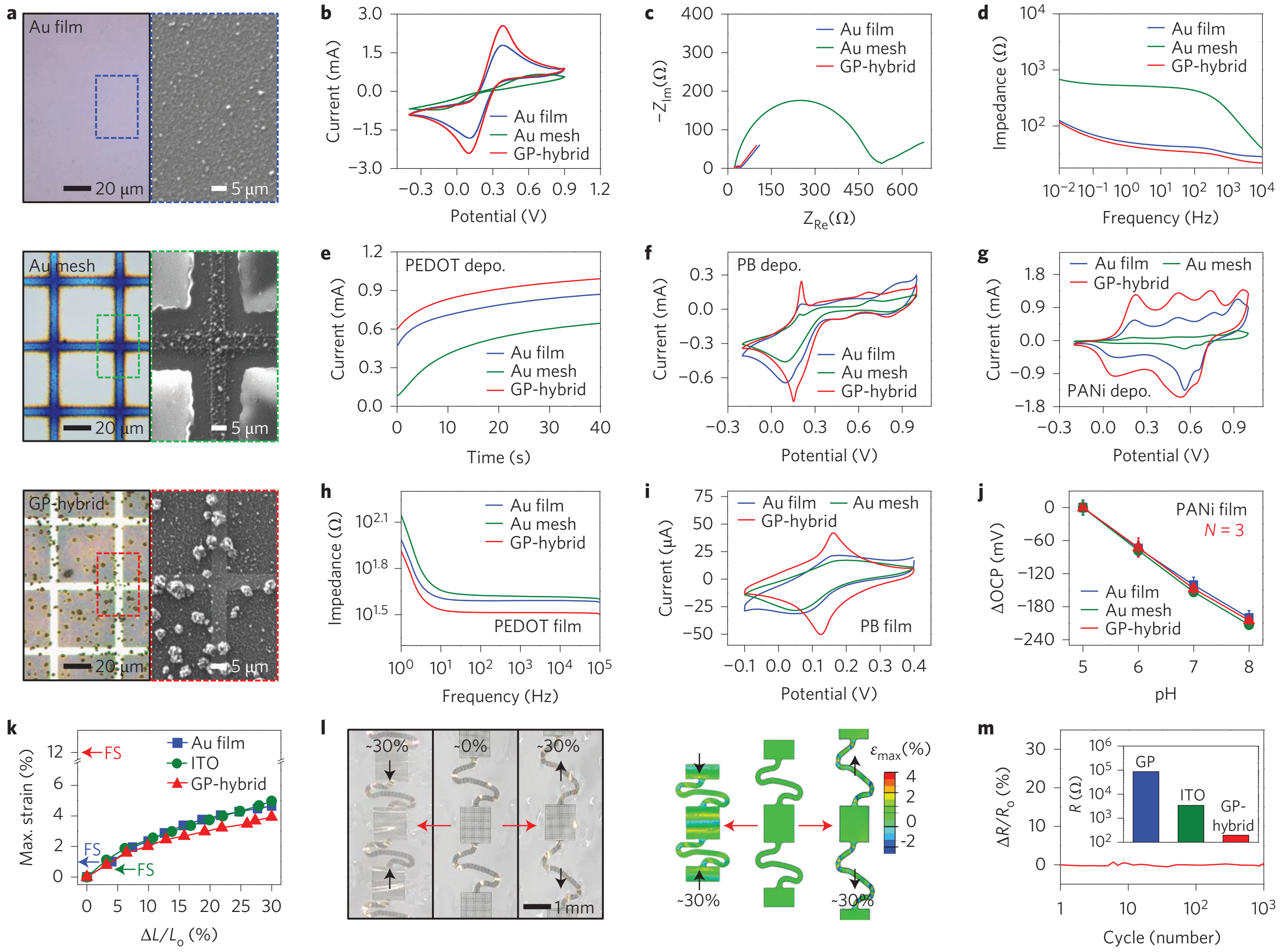

Figure 2 | Electrochemical, mechanical and electrical characterization of the Au mesh, Au film and GP-hybrid. a, Optical (left) and SEM (right) images of the Au film (top), Au mesh (middle) and GP-hybrid (bottom) after the PEDOT electrodeposition. **b**, CV plots of the electrodes in PBS with $Fe(CN)_6^{3-/4-}$ (scan rate: 0.1 V s^{-1} with a commercial Ag/AgCl electrode). **c**, Nyquist plots of the electrodes in PBS with $Fe(CN)_6^{3-/4-}$ at the equilibrium potential. **d**, Bode plots of the electrodes in PBS with $Fe(CN)_6^{3-/4-}$ at the equilibrium potential. **e**, Amperometric curves of the electrodes during the PEDOT electrodeposition process (initial potential: 1.25 V versus a commercial Ag/AgCl electrode). **f**, CV plots of the electrodes during the PB electrodeposition process (scan rate: 0.1 V s^{-1} with a commercial saturated calomel electrode). **g**, CV plots of electrodes during the PANi electrodeposition process (scan rate: 0.1 V s^{-1} with a commercial Ag/AgCl electrode). **h**, Bode plots of the electrodes in PBS after electrodeposition of PEDOT. **i**, CV plots of the electrodes in PBS after electrodeposition of PB (scan rate: 0.1 V s^{-1} with a commercial Ag/AgCl electrode). **j**, pH-dependent OCP changes in the electrodes after electrodeposition of PANi ($N = 3$, error bars show the standard deviation, OCP versus a commercial Ag/AgCl electrode). **k**, Comparison of the maximum induced strain in the rectangular island of the GP-hybrid electrode under the 0–30% stretching with that of other electrodes (Au film and indium tin oxide (ITO)). The arrows show the fracture strain (FS) of each electrode material. **l**, Optical images (left) and corresponding FEM strain distribution analysis results (right) of the GP-hybrid interconnection under compressed (left red arrow, ~30% compressed), undeformed and stretched (right red arrow, ~30% stretched) states. ε_{max}, maximum amount of strain. **m**, Relative resistance changes of the GP-hybrid electrode after the cyclic stretching test. The inset compares the resistance of the GP-hybrid electrode with that of other transparent electrodes (graphene and ITO).

(Supplementary Fig. 5c,d). This large electrochemically active surface area of the GP-hybrid electrode is consistent with the nanostructured topography in visual observations (optical and SEM images), which corroborates its superb characteristics. In contrast, electrochemical characterization of the undoped CVD graphene shows negligible redox reactions and high impedances due to its low electrochemical activity (Supplementary Fig. 6a–c).

These electrochemical properties of the GP-hybrid electrode are further highlighted through functionalization, which is supported by enhanced electrochemical activities during and after the electrodeposition of functional materials. Figure 2e–g shows larger electrical current amplitudes and sharper characteristic peaks of the GP-hybrid during the controlled electrodeposition process of PEDOT, Prussian Blue (PB), and polyaniline (PANi). The electrode of the GP-hybrid exhibits excellent electrochemical interactions with each monomer. The resulting GP-hybrid film shows better electrochemical performances, including lower interfacial impedance of the PEDOT/GP-hybrid (Fig. 2h and Supplementary Fig. 7a) and more prominent characteristic redox peaks of the PB/GP-hybrid (Fig. 2i and Supplementary Fig. 7b) compared with others. However, the pH-dependent open circuit potential (OCP) of the PANi/GP-hybrid shows comparable trends to that of the Au film and Au mesh (Fig. 2j and Supplementary Fig. 7c). The GP-hybrid clearly improves impedance-based (PEDOT) and charge-transfer-based (PB) electrochemical activities, for which reactions occur on the surface. However, the OCP depends on bulk properties of the PANi rather than the surface properties and thereby similar results are observed.

High conductivity and mechanical robustness are important for efficient charge/signal injection into and extraction from

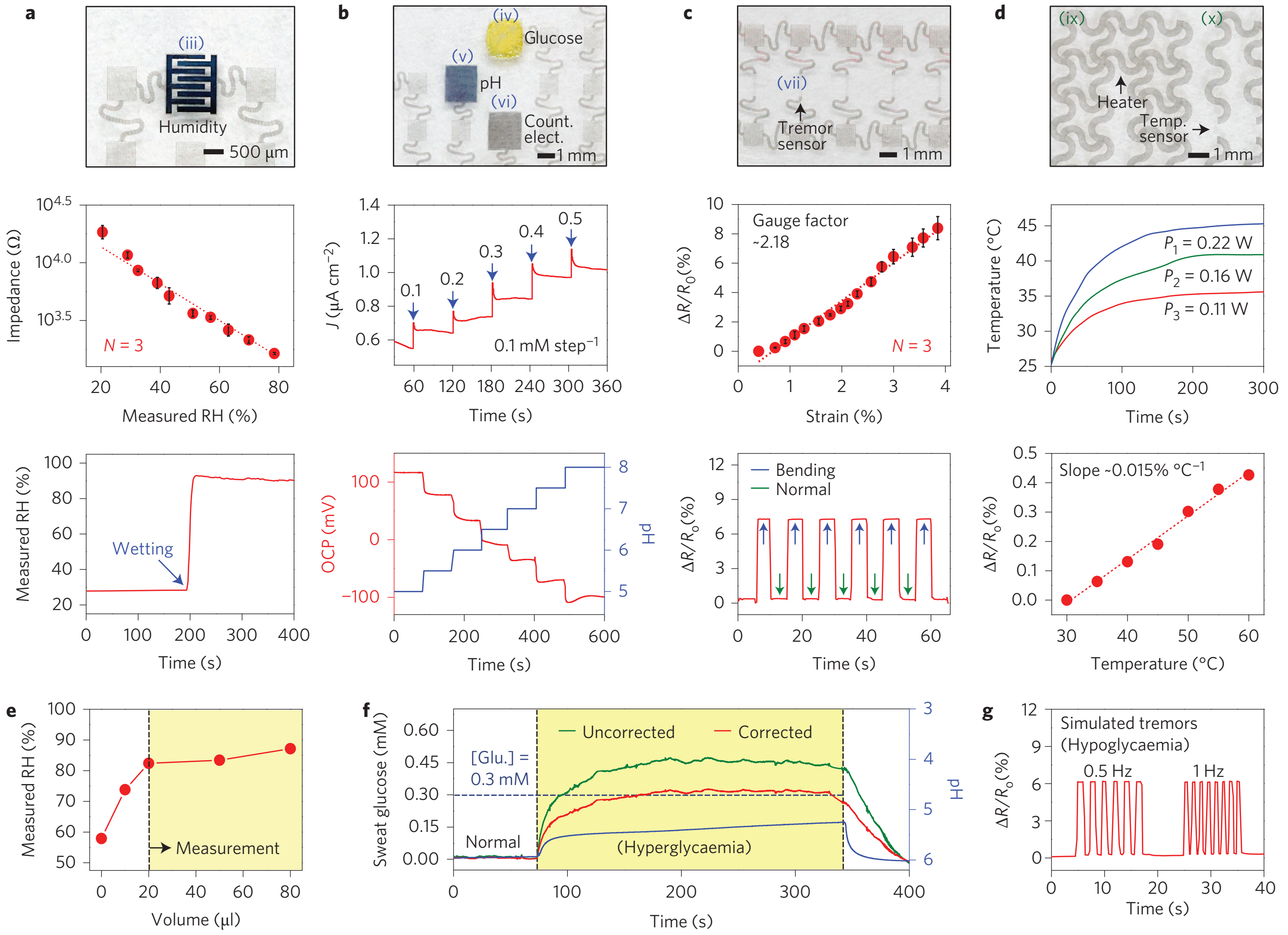

Figure 3 | Electrochemical and electrical characterization of individual devices and their combined operation *in vitro.* a, Optical image (top) and calibration curve (middle; *N* = 3, error bars show the standard deviation) of the humidity sensor. The bottom plot shows the measurement of impedance changes under wetting. **b**, Optical image (top) and calibration curve of the glucose sensor (middle; blue arrows indicate glucose concentrations in each step; initial potential: −0.05 V versus a solid-state Ag/AgCl electrode) and pH sensor (bottom; OCP versus a solid-state Ag/AgCl electrode). **c**, Optical image (top) and calibration curve (middle; *N* = 3, error bars show the standard deviation) of the tremor sensor (strain gauge). The bottom plot shows the measurement of strain changes during repeated bending deformations. **d**, Optical image (top) and characterization curves of the heater (middle; output temperature profiles at different power values (P_1–P_3)) and temperature sensor (bottom; the slope indicates sensitivity of the temperature sensor). **e**, Measurement of humidity changes with the application of different volumes of artificial sweat. When measured RH is over 80% (yellow region), sensors operate reliably. **f**, Monitoring of glucose (initial potential: −0.05 V versus a solid-state Ag/AgCl electrode) and pH (OCP versus a solid-state Ag/AgCl electrode) changes *in vitro* under hyperglycaemia in artificial sweat (0.3 mM sweat glucose level corresponding to 300 mg dl^{-1} blood glucose level). **g**, The tremor sensor in the patch detects tremors similar to those experienced by hypoglycaemic patients. Under hypoglycaemic conditions, physiological tremors occur with frequency over 1 Hz.

electrochemical cells. Mechanical robustness under various deformations is another important requirement of skin-based wearable systems[29,30]. In addition to the intrinsic softness of graphene (Fig. 2k; arrows show the typical fracture strain of each material[3,31,32]), electrodes that use serpentine designs significantly enhance mechanical deformability (Fig. 2l, left). To prevent mechanical fractures in the Au mesh, we used serpentine designs[33,34]. The neutral mechanical plane[29,30] and ultrathin design[35–37] further increase the tolerance to mechanical deformations. These materials and design strategies minimize the induced strain occurring during deformations. These experimental results are confirmed with finite element modeling (FEM) analysis (Fig. 2l, right). See Supplementary Section 1.2 and Supplementary Fig. 8 for more details about the mechanical properties. In our design, the serpentine Au mesh subjacent to gold-doped CVD graphene enhances the electrical conductivity in comparison with conventional transparent electrodes while minimizing mechanical fractures during a cyclic stretching test (Fig. 2m and its inset). An extra important advantage of the GP-hybrid is in the optical transparency, providing the natural skin-like appearance of the diabetes patch (Supplementary Fig. 9).

Characterization of the diabetes patch *in vitro*

After the fabrication of the interconnected array layout on a handle substrate, the device is transfer-printed onto a thin silicone patch, followed by the selective, patterned electrochemical functionalization for GP-hybrid sensors (Supplementary Fig. 10). The stepwise selective electrodeposition of each functional material prevents cross-contamination (Supplementary Fig. 11 and Supplementary Section 1.3). The heater, tremor sensor (strain gauge) and temperature sensor are fabricated by the resistance modulation of graphene and the Au mesh (Fig. 1b).

The sensors for humidity, glucose/pH and tremor and the heater/temperature sensor are described in Fig. 3. The humidity sensor monitors the relative humidity (RH) changes based on impedance changes in the interdigitated PEDOT electrodes to make sure a sufficient amount of sweat is present on the skin (Fig. 3a and

Supplementary Fig. 12a). The glucose and pH sensors measure electrochemical signal changes of the PB/GP-hybrid by the reduction of H_2O_2 generated from the glucose oxidase and those of the PANi/GP-hybrid by pH changes, respectively, in conjunction with the solid-state Ag/AgCl counter electrode (Fig. 3b and Supplementary Fig. 12b–d). The glucose sensor is calibrated before its first use and tested in the glucose concentration range between 10 μM and 0.7 mM (Fig. 3b middle and Supplementary Fig. 13a–c). These glucose concentrations correspond to typical sweat glucose concentrations of hypoglycaemic and hyperglycaemic patients as well as normal people[23–25]. The glucose sensor is found to be stable under mechanical deformations and maintains its sensitivity under various motions (Supplementary Fig. 13b). The glucose sensor reacts specifically to glucose in the presence of other biomolecules contained in the sweat (for example, lactate, ascorbic acid and uric acid; Supplementary Fig. 13d,e). The glucose oxidase in the current device setting is active at least for a day under ambient conditions and for several days depending on storage conditions (see Supplementary Fig. 13f and Methods). The low operation potential (initial potential: −0.05 V versus the solid-state Ag/AgCl electrode) of the glucose sensor prevents electrochemical interference.

The pH sensor is calibrated with stepwise pH changes using standard pH buffer solutions and is stably operated under deformations (Fig. 3b bottom and Supplementary Fig. 14a,b). The pH sensor is used to correct the pH-dependent deviation of the enzyme-based glucose sensor. The glucose oxidase (GOx) is affected by pH changes in the sweat. The sweat pH is typically lower than the neutral condition (that is, pH = 7) due to the metabolic lactic acid secretion during muscle movements (Supplementary Fig. 14c) and varies among human subjects. The time-dependent stability of the glucose sensor is also estimated. The glucose sensor measures the glucose level reliably for 6 h without further calibrations (Supplementary Fig. 15a). The tremor sensor (strain gauge) is calibrated and successfully measures cyclic strain changes (Fig. 3c). The heater and temperature sensor are calibrated (Fig. 3d) and used in the drug delivery process.

The combined operation of these sensors using the artificial sweat *in vitro* is shown in Fig. 3e–g. First, the humidity sensor monitors RH and determines the starting point for glucose and pH sensing, which are stabilized at RH of >80% (Fig. 3e). The diabetes patch needs at least 20 μl of human sweat for measurement of the glucose concentration. No disturbance is found in larger volumes of sweat (Supplementary Fig. 15b,c). The glucose and pH sensors measure real-time changes in glucose and pH. Simulated hyperglycaemia (0.3 mM sweat glucose level corresponding to a 300 mg dl^{-1} blood glucose level)[23] is then successfully detected, as shown in Fig. 3f. Hyperglycaemia is defined when the blood glucose level is above 126 mg dl^{-1} under fasting[38]. However, owing to continuous pH changes (blue), the efficiency of GOx and thereby the sensitivity of the glucose sensor is susceptible to error. Therefore, glucose monitoring with real-time correction using *in situ* pH measurements (red) agrees much better with the real glucose concentration of the artificial sweat (dotted line, 0.3 mM) than the uncorrected one (green). The temperature dependency of the glucose and pH sensors are estimated. The sensitivity of the glucose sensor is slightly decreased as the temperature decreases, whereas the sensitivity of the pH sensor is similar at various temperatures (Supplementary Fig. 16a,b and Supplementary Section 1.4). Our diabetes patch, therefore, provides more reliable sensing performances than previous devices due to systematic correction of sweat glucose measurements based on pH and temperature monitoring (Supplementary Section 1.5). The potential interactions of the glucose sensor with common drugs (aspirin, Tylenol and Metformin) are also estimated. Their influences on glucose sensing are minimal (Supplementary Fig. 16c and Supplementary Section 1.4). The wearable tremor sensor detects simulated tremors that could possibly be induced in hypoglycaemic states, where physiological tremors occur with a frequency over 1 Hz (Fig. 3g)[39]. After comparison with preprogrammed thresholds of the acceptable glucose concentration that are determined by a family doctor, the real-time glucose monitoring data can trigger the heater embedded in the patch to thermally activate the drug-loaded microneedles. When the heater is turned off, the microneedles coated with the PCM remain inactive.

Demonstration of sweat-based monitoring and therapy *in vivo*

Integrated system-level demonstrations of the wearable diabetes patch *in vivo* are described in Fig. 4. The diabetes patch is laminated on the human skin and is electrically coupled to a portable electrochemical analyser (Supplementary Fig. 2), which in turn wirelessly transfers data to remote mobile devices (for example, a smartphone or tablet computer) and supplies power to the patch (Fig. 4a). Sweat-based glucose monitoring begins on sweat generation (Fig. 4b and Supplementary Fig. 17a). The humidity sensor monitors the increase in RH. It takes ~15 min on average (10–20 min) for the sweat-uptake layer of the patch to collect sweat and thereby to reach a RH over 80% for measurements (Supplementary Section 1.6). The glucose and pH measurements are initiated after the RH reaches 80% (Fig. 4c).

Two healthy volunteers (both men in their twenties) with no medical history of heart problems or diabetes participated in the study. All subjects were informed of risks and benefits and provided informed consent. The pH of human sweat is different among subjects, as are the subject's physiological and/or environmental conditions (Fig. 4d). The pH sensor monitors these changes/differences and corrects the pH-dependent glucose measurements *in situ*. Daily glucose monitoring data *in vivo* are presented in Fig. 4e. Sweat glucose concentrations measured by the diabetes patch (red circles) and a commercial glucose assay kit (Cayman chemical, USA; red dots) are well matched. In addition, changes in the sweat glucose concentration (red, left y axis) are well correlated with those of the blood glucose concentration (blue, right y axis) (correlation factor: ~0.017; the ratio of the sweat glucose concentration to the blood glucose concentration). Blood glucose concentrations are measured by a commercial glucose meter (Accu-chek performa, Roche, Switzerland). A statistical analysis confirms the reliable correlation between sweat glucose data from the diabetes patch and those from the commercial glucose assay ($P < 0.001$, $R^2 = 0.89$) (Supplementary Fig. 17b) as well as the correlation between the sweat glucose data from the diabetes patch and blood glucose data from the commercial glucose meter ($P < 0.001$, $R^2 = 0.83$) (Supplementary Fig. 17c). The pH correction effect on the glucose monitoring is shown in Fig. 4f. Corrections using the measured pH (red) provide more accurate glucose monitoring data than those without corrections (orange) compared with the real glucose concentration measured by the glucose assay (green). Another practical advantage of the diabetes patch is that the sensitivities of the glucose and pH sensors are barely affected after multiple lamination/delamination processes for reuse (Fig. 4g and Supplementary Fig. 17d,e). The glucose and pH sensors also show similar sensitivities in multiple sensors (Supplementary Fig. 17f).

Detection of hyperglycaemia triggers the thermal actuation of the drug-loaded microneedles. Details of the microneedle fabrication process are provided in Supplementary Fig. 18 and the Methods. A large-scale view of the fabricated microneedles is presented in Supplementary Fig. 19a. Microneedles are composed of a bioresorbable polymer (polyvinyl pyrrolidone (PVP)[23,24]) in combination with a pharmacological agent (Metformin[40]; Product #D150959, Sigma-Aldrich, USA). A thermally active bioresorbable coating layer of PCM (tridecanoic acid; Product #T0412, Tokyo Chemical Industry, Japan)[25] further protects the PVP/drug from moistures and/or biofluids below the transition temperature ($T_c = 41–42\,°C$), as shown in Fig. 4h. Thermal actuation above T_c melts the PCM and releases drug into the bloodstream (see Supplementary Section 1.7). Analysis using a high-performance liquid chromatograph (HPLC;

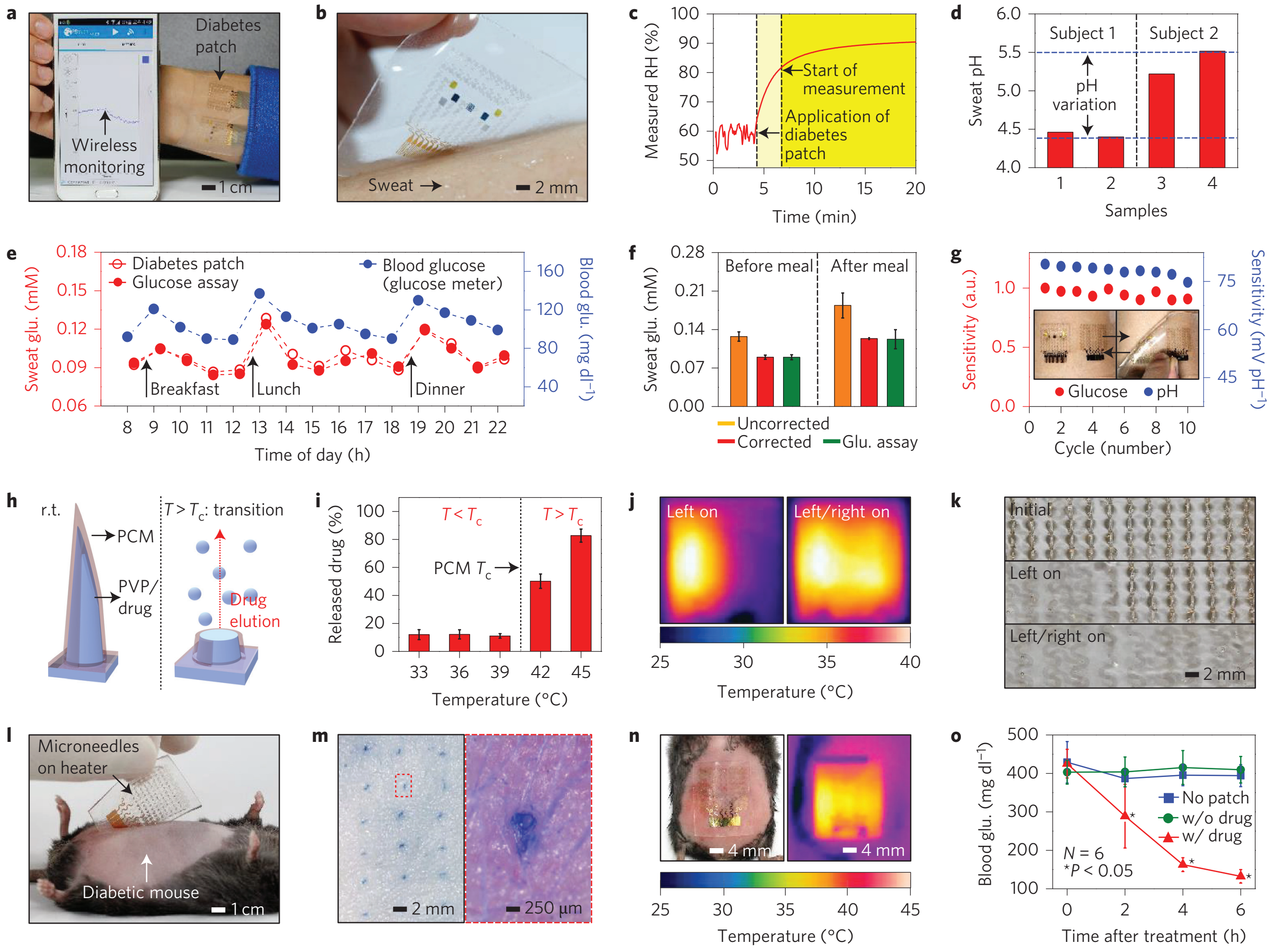

Figure 4 | Demonstration of the wearable diabetes monitoring and therapy system *in vivo*. a, Optical image of the integrated wearable diabetes monitoring and therapy system connected to a portable electrochemical analyser. The electrochemical analyser wirelessly communicates with external devices via Bluetooth. **b**, Optical image of the GP-hybrid electrochemical device array on the human skin with perspiration. **c**, RH measurement by the diabetes patch. **d**, Measurement of the pH variation in two human sweat samples from two subjects. **e**, One-day monitoring of glucose concentrations in the sweat and blood of a human (subject 2 in **d**). **f**, Comparison of the average glucose concentrations with the commercial glucose assay data in **e** before and after correction using the measured pH (error bars show the standard deviation). **g**, Plots showing the stable sensitivity of the glucose and pH sensors after multiple reuses of the patch. **h**, Schematic illustrations of bioresorbable microneedles. **i**, Drug release from the microneedles at different temperatures ($N = 3$, error bars show the standard deviation). **j**, Infrared camera images of multichannel heaters showing the stepwise drug release. **k**, Optical images of the stepwise dissolution of the microneedles. **l**, Optical image of the heater integrated with the microneedles, which is laminated on the skin near the abdomen of the db/db mouse. The hair on the skin was shaved off before treatment with the microneedles. **m**, Optical image (left) and its magnified view (right) of the db/db mouse skin stained with trypan blue to visualize the micro-sized holes made by the penetration of the microneedles. **n**, Optical (left) and infrared (right) camera images of the patch with the thermal actuation. **o**, Blood glucose concentrations of db/db mice for the treated group (with the drug) and control groups (without the patch and without the drug). The error bars show the standard deviation in each group and small P values show that the results are statistically reliable. The asterisks indicate significant difference ($P < 0.05$) between the treated (red) and the non-treated group (blue and green) on each time point.

Ultimate 3000, Dionex, USA) shows the elution of drug at elevated temperatures (>41 °C; Fig. 4i and Supplementary Fig. 19b). The integrated temperature sensor monitors temperature changes on the skin and prevents any overheating (Supplementary Fig. 19c). The patterned heating triggers drug release in a stepwise manner (two step release in Fig. 4j,k, and four step release in Supplementary Fig. 19d,e). By increasing the total area of the microneedles, the maximum number and/or amount of the drug deliveries can be increased (see Supplementary Section 1.7 for details).

Therapeutic effects are tested *in vivo* using 8- to 10-week-old diabetic (db/db) mice (Supplementary Fig. 20) using a genetically derived diabetic animal model. Treatment begins by laminating the patch on the skin near the abdomen of the db/db mouse (Fig. 4l). The microneedles penetrate through the surface of the skin, reaching the subcutaneous region, as shown in the optical images (Fig. 4m). Once the db/db mouse is treated with thermally actuated microneedles (optical and infrared camera image in Fig. 4n), the drug (Metformin) is released into the bloodstream. The experimental group treated with microneedles shows a significant suppression of blood glucose concentrations with respect to the control groups (Fig. 4o; $P < 0.05$, ANOVA with post hoc analysis). One can easily replace the used microneedles with new ones (Supplementary Fig. 21a,b). The drug-loading capacity of the microneedles can be further increased by using its backing layer[41–43] (Supplementary Fig. 21c). Treatment with Metformin through the skin is much more efficient than the digestive system[44] because the drug is directly introduced into metabolic circulation through the skin[45]. More studies into transdermal drug delivery for human patients are needed in the future. The Metformin is effective not only for treating diabetic patients, but also for people at risk of the diabetes for preventive purposes[46], which maximizes the utility of the current diabetes patch.

Conclusions

We report soft materials, device designs and system integration strategies for a new class of diabetes monitoring and therapy devices based on functionalized CVD graphene. Graphene biochemical sensors with solid-state Ag/AgCl counter electrodes show enhanced electrochemical activity, sensitivity and selectivity in detecting important biomarkers contained in human sweat. The GP-hybrid interconnections and physical sensors efficiently transmit the signal through the stretchable array and supplement electrochemical sensors, respectively. The orchestrated monitoring of biomarkers and physiological cues with sweat control and transcutaneous drug delivery achieves a closed-loop, point-of-care treatment for diabetes. The detection of RH over a critical point due to sweat activates the glucose sensing, which is corrected by simultaneous measurement of pH and temperature. High glucose concentration recordings trigger the embedded heaters to dissolve PCM and as a result, bioresorbable microneedles release Metformin as a feedback transdermal drug delivery to the glucose sensing. The use of intrinsically soft materials enhances the conformal integration of devices with the human skin and thus improves the effectiveness of biochemical sensors and drug delivery. The wireless connectivity further highlights the practical applicability of the current patch system. These advances using nanomaterials and devices provide new opportunities for the treatment of chronic diseases such as diabetes mellitus.

Methods

Methods and any associated references are available in the online version of the paper.

Received 18 May 2015; accepted 17 February 2016;

References

1. Kim, K. S. *et al.* Large-scale pattern growth of graphene films for stretchable transparent electrodes. *Nature* **457,** 706–710 (2009).
2. Bae, S. *et al.* Roll-to-roll production of 30-inch graphene films for transparent electrodes. *Nature Nanotech.* **5,** 574–578 (2010).
3. Lee, C., Wei, X., Kysar, J. W. & Hone, J. Measurement of the elastic properties and intrinsic strength of monolayer graphene. *Science* **321,** 385–388 (2008).
4. Schwierz, F. Graphene transistors. *Nature Nanotech.* **5,** 487–496 (2010).
5. Bonaccorso, F., Sun, Z. & Ferrari, A. C. Graphene photonics and optoelectronics. *Nature Photon.* **4,** 611–622 (2010).
6. Sun, Q. *et al.* Transparent, low-power pressure sensor matrix based on coplanar-gate graphene transistors. *Adv. Mater.* **26,** 4735–4740 (2014).
7. Lee, W. H. *et al.* Transparent flexible organic transistors based on monolayer graphene electrodes on plastic. *Adv. Mater.* **23,** 1752–1756 (2011).
8. Chung, C. *et al.* Biomedical applications of graphene and graphene oxide. *Acc. Chem. Res.* **46,** 2211–2224 (2011).
9. Duy, L. T. *et al.* High performance three-dimensional chemical sensor platform using reduced graphene oxide formed on high aspect-ratio micro-pillars. *Adv. Funct. Mater.* **25,** 883–890 (2015).
10. Kim, D.-J. *et al.* Electrical graphene aptasensor for ultra-sensitive detection of anthrax toxin with amplified signal transduction. *Small* **9,** 3352–3360 (2013).
11. Park, D.-W. *et al.* Graphene-based carbon-layered electrode array technology for neural imaging and optogenetic applications. *Nature Commun.* **5,** 5258 (2014).
12. Han, T.-H. *et al.* Extremely efficient flexible organic light-emitting diodes with modified graphene anode. *Nature Photon.* **6,** 105–110 (2012).
13. Xu, L. *et al.* 3D multifunctional integumentary membranes for spatiotemporal cardiac measurements and stimulation across the entire epicardium. *Nature Commun.* **5,** 3329 (2014).
14. Guinovart, T. *et al.* A potentiometric tattoo sensor for monitoring ammonium in sweat. *Analyst* **138,** 7031–7038 (2013).
15. Jia, W. *et al.* Electrochemical tattoo biosensors for real-time noninvasive lactate monitoring in human perspiration. *Anal. Chem.* **85,** 6553–6560 (2013).
16. Bandodkar, A. J. *et al.* Tattoo-based noninvasive glucose monitoring: a proof-of-concept study. *Anal. Chem.* **87,** 394–398 (2015).
17. Tee, B. C.-K. *et al.* An electrically and mechanically self-healing composite with pressure- and flexion-sensitive properties for electronic skin applications. *Nature Nanotech.* **7,** 825–832 (2012).
18. Schwartz, G. *et al.* Flexible polymer transistors with high pressure sensitivity for application in electronic skin and health monitoring. *Nature Commun.* **4,** 1859 (2013).
19. Minev, I. R. *et al.* Electronic dura mater for long-term multimodal neural interfaces. *Science* **347,** 159–163 (2015).
20. Gerratt, A. P. *et al.* Elastomeric electronic skin for prosthetic tactile sensation. *Adv. Funct. Mater.* **25,** 2287–2295 (2015).
21. Son, D. *et al.* Multifunctional wearable devices for diagnosis and therapy of movement disorders. *Nature Nanotech.* **9,** 397–404 (2014).
22. Kim, J. *et al.* Stretchable silicon nanoribbon electronics for skin prosthesis. *Nature Commun.* **5,** 5747 (2014).
23. Moyer, J., Wilson, D., Finkelshtein, I., Wong, B. & Potts, R. Correlation between sweat glucose and blood glucose in subjects with diabetes. *Diabetes Technol. Ther.* **14,** 398–402 (2012).
24. Sakaguchi, K. *et al.* Evaluation of a minimally invasive system for measuring glucose area under the curve during oral glucose tolerance tests: usefulness of sweat monitoring for precise measurement. *J. Diabetes Sci. Tehcnol.* **7,** 678–688 (2013).
25. Olarte, O., Chilo, J., Pelegri-Sebastia, J., Barbé, K. & Moer, W. V. Glucose detection in human sweat using an electronic nose. *Conf. Proc. IEEE Eng. Med. Biol. Soc.* **2013,** 1462–1465 (2013).
26. Sullivan, S. P. *et al.* Dissolving polymer micro-needle patches for influenza vaccination. *Nature Med.* **16,** 915–920 (2010).
27. Sullivan, S. P. *et al.* Minimally invasive protein delivery with rapidly dissolving polymer microneedles. *Adv. Mater.* **20,** 933–938 (2008).
28. Hyun, D. C. *et al.* Emerging applications of phase-change materials (PCMs): teaching an old dog new tricks. *Angew. Chem. Int. Ed.* **53,** 3780–3795 (2014).
29. Xu, S. *et al.* Soft microfluidic assemblies of sensors, circuits, and radios for the skin. *Science* **344,** 70–74 (2014).
30. Jang, K.-I. *et al.* Soft network composite materials with deterministic and bio-inspired designs. *Nature Commun.* **6,** 6566 (2015).
31. Lacour, S. P. *et al.* Stretchable gold conductors on elastomeric substrates. *Appl. Phys. Lett.* **82,** 2404–2406 (2003).
32. Cao, Q. *et al.* Highly bendable, transparent thin-film transistors that use carbon-nanotube-based conductors and semiconductors with elastomeric dielectrics. *Adv. Mater.* **18,** 304–309 (2006).
33. Guo, C. G. *et al.* Highly stretchable and transparent nanomesh electrodes made by grain boundary lithography. *Nature Commun.* **5,** 3121 (2014).
34. Vandeparre, H. *et al.* Localization of folds and cracks in thin metal films coated on flexible elastomer foams. *Adv. Mater.* **25,** 3117–3121 (2013).
35. Kaltenbrunner, M. *et al.* An ultra-lightweight design for imperceptible plastic electronics. *Nature* **499,** 458–463 (2013).
36. Sekitani, T., Zschieschang, U., Klauk, H. & Someya, T. Flexible organic transistors and circuits with extreme bending stability. *Nature Mater.* **9,** 1015–1022 (2010).
37. Sekitani, T. *et al.* Organic nonvolatile memory transistors for flexible sensor arrays. *Science* **326,** 1516–1519 (2009).
38. Ismail-Beigi, F. Glycemic management of type 2 diabetes mellitus. *N. Engl. J. Med.* **366,** 1319–1327 (2012).
39. Hallett, M. Classification and treatment of tremor. *J. Am. Med. Assoc.* **266,** 1115–1117 (1991).
40. Bailey, C. J., Path, M. R. C. & Turner, R. C. Metformin. *N. Engl. J. Med.* **334,** 574–579 (1996).
41. Lee, J. W., Park, J.-H. & Prausnitz, M. R. Dissolving microneedles for transdermal drug delivery. *Biomaterials* **29,** 2113–2124 (2008).
42. Kochhar, J. S. *et al.* Microneedle integrated transdermal patch for fast onset and sustained delivery of lidocaine. *Mol. Pharm.* **10,** 4272–4280 (2013).
43. Cai, B., Xia, W., Bredenberg, S. & Engqvist, H. Self-setting bioceramic microscopic protrusions for transdermal drug delivery. *J. Mater. Chem. B* **2,** 5992–5998 (2014).
44. Scarbrough, C. A., Scarbrough, S. S. & Shubrook, J. Transdermal delivery of metformin. US patent 13/504,799 (2012).
45. Prausnitz, M. R. & Langer, R. Transdermal drug delivery. *Nature Biotechnol.* **26,** 1261–1268 (2008).
46. Knowler, W. C. *et al.* Reduction in the incidence of type 2 diabetes with lifestyle intervention or metformin. *N. Engl. J. Med.* **346,** 393–403 (2002).

Acknowledgements

This work was supported by IBS-R006-D1.

Author contributions

H.L., T.K.C., Y.B.L. and D.-H.K. designed the experiments. H.L., T.K.C., Y.B.L., H.R.C., L.W., H.J.C., T.D.J., N. L., T.H., S.H.C. and D.-H.K. performed experiments and analysis. H.L., T.K.C., Y.B.L., H.J.C., R. G., T.D.J., N. L., T.H., S.H.C. and D.-H.K. wrote the paper.

Additional information

Supplementary information is available in the online version of the paper. Reprints and permissions information is available online at www.nature.com/reprints. Correspondence and requests for materials should be addressed to D.-H.K.

Competing financial interests

The authors declare no competing financial interests.

Methods

Fabrication process of the device array. The device fabrication begins with the spin-coating of the epoxy layer (~1.5 µm; SU8-2, Microchem, USA) on a nickel sacrificial layer (~50 nm; thermal evaporation) deposited on a silicon handle wafer. After curing of the coated epoxy, the bottom epoxy layer is patterned using photolithography. Thermal evaporation is used to form the Cr/Au (~7 nm/~70 nm) film, which is patterned as the Au mesh interconnects using photolithography and wet etching. The graphene, synthesized on a Cu foil (Product #46365, Alfa Aesar, USA) through the CVD process, is transferred and patterned. Finally, the device is encapsulated with another epoxy layer. The fabricated device is transfer-printed onto a PDMS substrate (Sylgard 184, Dow Chemical, USA) after the wet etching of the sacrificial nickel layer.

Electrochemical characterization of the electrodes. The a.c. impedance, CV, galvanostatic method, amperometric *I*–*t* curve and OCP measurements are performed using an electrochemical analyser (CHI660E, CH instrument, USA). Characterization of the electrodes and functional materials (Fig. 2b–j) is carried out using the three-electrode method with the reference electrode (commercial Ag/AgCl electrode, saturated calomel electrode (SCE), Ag electrode), Pt counter electrode and fabricated working electrode (designed area is 1 cm^2 for intrinsic characterization of each electrode).

Selective functionalization of electrochemical devices. Selective functionalization is carried out through electrodeposition using the three-electrode method for the electrodes described above. The process is as follows:

(i) Au doping. Before the selective functionalization, Au doping on the bilayer electrode of Au mesh and graphene is proceeded by the treatment with 20 mM $AuCl_3$ (Product #43360, Alfa Aesar, USA) aqueous solution for 5 min. After Au doping, active sites are gently washed with water.
(ii) Ag/AgCl electrodeposition. An aqueous solution of 5 mM $AgNO_3$ (Product #209139, Sigma-Aldrich, USA) and 1 M KNO_3 (Product #P8394, Alfa Aesar, USA) is prepared. The GP-hybrid electrode is dipped into the prepared solution. The potential is swept from −0.9 to 0.9 V versus an Ag electrode for 20 segments at a scan rate of 0.1 V s^{-1}. For chlorination, the electrode is dipped in an aqueous solution of 0.1 M KCl (Product #P5405, Sigma-Aldrich, USA) and 0.01 M HCl (Product #H1758, Sigma-Aldrich, USA). The potential is swept from −0.15 to 1.05 V versus SCE for 4 segments at a scan rate of 0.05 V s^{-1}.
(iii) PEDOT electrodeposition. A solution of 0.01 M 3,4-ethylenedioxythiophene (Product #483028, Sigma-Aldrich, USA) and 0.1 M $LiClO_4$ (Product #271004, Sigma-Aldrich, USA) in acetonitrile (Product #271004, Sigma-Aldrich, USA) is prepared. The GP-hybrid electrode is dipped into the solution and the galvanostatic electrodeposition is performed with 0.5 mA of anodic current (potential versus commercial Ag/AgCl electrode) for 40 s. PEDOT deposition starts when the potential is higher than 1.2 V.
(iv) PANi electrodeposition. An aqueous solution of 0.1 M aniline (Product #242284, Sigma-Aldrich, USA) in 1 M HCl is prepared. The GP-hybrid electrode is dipped into the solution and the potential is swept from −0.2 to 1 V versus a commercial Ag/AgCl electrode for 40 segments at a scan rate of 0.1 V s^{-1}.
(v) PB electrodeposition. An aqueous solution of 0.1 M KCl, 5 mM $K_3[Fe(CN)_6]$ (Product #P702587, Sigma-Aldrich, USA) and 5 mM $FeCl_3$ (Product #236489, Sigma-Aldrich, USA) in 0.01 M HCl is prepared. The GP-hybrid electrode is dipped into the solution and the potential is swept from −0.2 to 1 V versus SCE for three segments at a scan rate of 0.1 V s^{-1}.
(vi) Drop-casting of GOx on glucose sensor and Nafion passivation. A solution of 0.1 M KCl and 0.5 g ml^{-1} GOx (Product #G7141, Sigma-Aldrich, USA) is prepared in 1× PBS (Dulbecco's phosphate-buffered saline, WELGENE Inc., Republic of Korea). A 2 µl aliquot of the solution is drop-casted on the PB/GP-hybrid twice. After the electrodes are dried, Nafion (Product #309389, Sigma-Aldrich, USA) is drop-casted on the humidity sensor (2 µl) and other sensors (10 µl).

Characterization of the humidity sensor. The humidity sensor is calibrated using the a.c. impedance method. Measurements are performed using the two-electrode method with PEDOT/GP-hybrid interdigital electrodes. RH is controlled by introducing a mixed stream of dry nitrogen and deionized water vapour into the test chamber, and measured using a commercial humidity meter (Center310, Center, Taiwan). The humidity sensor is calibrated between 20% and 80% RH at 100 Hz (Fig. 3a middle). For real-time monitoring of humidity, the impedance-time measurements are performed at 100 Hz (Fig. 3a bottom).

Characterization of the glucose sensor. The glucose sensor is characterized under ambient air conditions by using amperometric *I*–*t* curves (initial potential: −0.05 V versus the solid-state Ag/AgCl electrode) according to the following tests.

- Calibration and stretching test. The glucose sensor is calibrated in the glucose concentration range between 10 µM and 0.7 mM (Supplementary Fig. 13a,b). For the stretching test, measurements are performed from 0 to 0.7 mM under 10%, 20% and 30% applied strains (Supplementary Fig. 13b).
- Selectivity test. The selectivity of the sensor is tested by the stepwise addition of 0.3 mM glucose (Product #G7141, Sigma-Aldrich, USA), 4 mM lactate (Product #69775, Sigma-Aldrich, USA), 10 µM ascorbic acid (Product #A7506, Sigma-Aldrich, USA), 59 µM uric acid (Product #U2625, Sigma-Aldrich, USA) and 0.5 mM glucose every 60 s (Supplementary Fig. 13d).
- pH and temperature dependency test. The pH dependency of the glucose sensor is estimated with solutions of 0 to 0.5 mM glucose at different pH values (Supplementary Fig. 14c). The temperature dependency of the glucose sensor is estimated at 5 °C, 15 °C and 25 °C (Supplementary Fig. 16a).
- Time dependent stability test. The stability of the glucose sensing in artificial sweat (0.3 mM) for 6 h with a 2 h interval is estimated at room temperature (Supplementary Fig. 15a). For the long-term stability test over several days, the glucose sensor is tested at room temperature and stored at 4 °C when not in use (Supplementary Fig. 13f).
- Drug interaction test. The effects of drug interactions on the sensitivity of the glucose sensor is estimated in a series of test solutions that contain glucose and common drugs (Supplementary Fig. 16c): glucose only (control), a mixture of glucose and 20 µg ml^{-1} acetaminophen (Tylenol; Product #A7085, Sigma-Aldrich, USA), a mixture of glucose and 100 µg ml^{-1} acetylsalicylic acid (Aspirin; Product #A5376, Sigma-Aldrich, USA) and a mixture of glucose and 100 µg ml^{-1} Metformin (Product #D150959, Sigma-Aldrich, USA).

Characterization of the pH sensor. pH-dependent changes in the zeta potential of the PANi/GP-hybrid are measured using an electrokinetic analyser (SurPASS, Anton Paar, USA; Supplementary Fig. 12d, bottom). The pH sensor is characterized under ambient air conditions using real-time OCP measurements with an electrochemical analyser. The two-electrode method with the PANi/GP-hybrid as the working electrode and the solid-state Ag/AgCl electrode as the counter electrode is used for the measurement. The pH sensor is calibrated using standard buffered pH solutions (buffered solutions pH from 5 to 8, Alfa Aesar, USA), as shown in Fig. 3b, bottom. The same measurement procedure is used for the stretching test under 10%, 20% and 30% applied strains (Supplementary Fig. 14a). The effect of temperature on the pH sensor is also tested by measuring the OCP change of the pH sensor using the standard buffered pH solutions at 5 °C, 15 °C and 25 °C (Supplementary Fig. 16b).

Characterization of the strain gauge, heater and temperature sensors. Changes in the resistance of the strain gauge are measured using a digital multimeter (USB-4065, National Instrument, USA). The temperature sensor is also calibrated using the same digital multimeter. The temperature is monitored using the fabricated temperature sensor while the heater is turned on. The temperature sensor data is compared with data from a commercial infrared camera (FLIR E8, FLIR, USA).

Wireless control of GP-hybrid electrochemical devices on the human skin. GP-hybrid electrochemical devices are connected to a portable electrochemical analyser (PalmSens3, Palm instrument B.V., Netherlands) using anisotropic conductive film (HST-9805-210, Elform, USA). The electrochemical analyser is controlled wirelessly using an Android application (PStouch from the Google Play Store) via Bluetooth. The humidity sensor first monitors RH changes inside the patch (Fig. 4c) during sweating on the human skin under warm conditions. When RH is over 80%, the glucose and pH sensors begin monitoring. It takes ~15 min on average, which correspond to the warm-up time. The relative current changes of the glucose sensor are converted into the sweat glucose level according to the calibration curve with pH-based corrections (Supplementary Fig. 14c).

Glucose level measurement process using glucose and pH sensors. Every glucose and pH sensor needs a two-step calibration process before their first use to ensure precise monitoring of glucose and pH levels. The glucose and pH sensors are first calibrated using artificial sweat solutions. For the glucose sensing, we used the amperometric measurement that gives a current (I) versus time (t) curve under constant potential (initial potential: −0.05 V versus the solid-state Ag/AgCl electrode). Relative current changes ($\Delta I/I_o$) are obtained at different glucose concentrations. Then $\Delta I/I_o$ will be converted into the glucose concentration based on the calibration curve (Supplementary Fig. 13a–c). For the pH sensing, the measured OCP is converted into the pH value using the calibration curve (Supplementary Fig. 14a,b). The measured pH value is then used to adjust the glucose concentration (Supplementary Fig. 14c). After the characterization of the glucose and pH sensors *in vitro*, the correlation factor between the glucose levels in the sweat and blood is obtained by measuring blood and sweat glucose concentrations *in vivo* (Supplementary Fig. 17c). In our device array, two glucose sensors are fabricated as a pair, as are the pH sensors. Therefore, glucose and pH sensing can be continued even if one of the paired sensors fails. If all paired sensors are not functioning properly, the whole integrated system should be replaced.

Fabrication process of PCM-coated bioresorbable microneedles. The intaglio PDMS mould for the microneedles is prepared using commercial microneedles (PAMAS, Prestige, Republic of Korea) as a master. The microneedles have a base diameter and height of 250 µm and 1 mm, respectively. A liquid mixture of vinyl pyrrolidone (Product #V3409, Sigma-Aldrich, USA), 1 wt% free-radical initiator (azobisisobutyronitrile; Product #A1482, Samchun, Republic of Korea) and 5 wt% Metformin (Product #D150959, Sigma-Aldrich, USA) is casted onto the mould. Then a device array is placed on top and the sample is dried in a vacuum chamber at room temperature. The sample is then radiated with the UV light for 30 min at room temperature using a 40 W UV lamp. After the full cross-linking, the microneedles are gently peeled off. Finally, PCM (tridecanoic acid, Product #T0412, Tokyo Chemical Industry, Japan) is spray-coated on the microneedles. For the replacement of the microneedles a slightly different fabrication process is used. In this process, a polyethylene naphthalate (PEN) film (thickness ~12 μm; Teonex Q51, Teijin Dupont Film, Japan) is used as a substrate.

***In vivo* animal experiment.** Female db/db mice at the age of 8 to 10 weeks that exhibit type II diabetes are used. Among 30 mice, 18 mice are selected at random without blinding. Drug-loaded microneedles on the heater and temperature sensor (Supplementary Fig. 19) are attached to the mouse skin with gentle pressure. Transcutaneous drug delivery is initiated by the thermal actuation. The changes in blood glucose concentration are measured using a commercial glucose meter (Accu-chek performa, Roche, Switzerland). The measured blood glucose levels from treated and control (no patch application and patch with drug-unloaded microneedles) groups are analysed using ANOVA with a post hoc method.

***In vitro* and *in vivo* characterization of microneedles.** Temperature-dependent drug release from PCM-coated microneedles is characterized by an HPLC (Ultimate 3000, Dionex, USA) *in vitro* (Fig. 4i and Supplementary Fig. 19b). The drug (Metformin; Product #D150959, Sigma-Aldrich, USA) is eluted in 4.3 min. The microneedles are dissolved by heating under droplets of artificial sweat. The changes in temperature are monitored using both a commercial infrared camera and the fabricated temperature sensor (Fig. 4j,n and Supplementary Fig. 19c). The therapeutic effect of the drug released from the microneedles is also tested *in vivo* with the db/db mouse model (Supplementary Fig. 20). The changes in blood glucose concentrations are monitored using a commercial glucose meter (Accu-chek performa, Roche, Switzerland), as shown in Fig. 4o.

Ethical approval for the animal experiment. All procedures are approved by the Institutional Animal Care and Use Committee (IACUC) of the Biomedical Research Institute of Seoul National University Hospital. All experiments are performed according to IACUC guidelines.

nature nanotechnology

SUPPLEMENTARY INFORMATION

DOI: 10.1038/NNANO.2016.38

A graphene-based electrochemical device with thermoresponsive microneedles for diabetes monitoring and therapy

Hyunjae Lee[1,2⊥], Tae Kyu Choi[1,2⊥], Young Bum Lee[1,2⊥], Hye Rim Cho[1,3], Roozbeh Ghaffari[4], Liu Wang[5], Hyung Jin Choi[6], Taek Dong Chung[7,8], Nanshu Lu[5], Taeghwan Hyeon[1,2], Seung Hong Choi[1,3], and Dae-Hyeong Kim[1,2]*

⊥These authors contributed equally to this work.

*To whom correspondence should be addressed.
E-mail: dkim98@snu.ac.kr

This supplementary information contains:
Supplementary Text, References, and Supplementary Figures

1. Supplementary Text

1.1. Electrode characterization using cyclic voltammograms and AC impedance measurements.

The electrochemical characterization of the Au film, Au mesh, and graphene-hybrid electrode in PBS with 10 mM $Fe(CN)_6^{3-/4-}$ are summarized in Supplementary Table 1. In cyclic voltammograms, the Au mesh shows peak currents at the higher potential than the others, suggesting that it has much higher charge transfer resistance (R_{ct}) for the redox reaction than the others, which is in good agreement with its Nyquist plot data (Fig. 2b,c). Under the same condition, the undoped CVD graphene film with and without Au mesh are electrochemically characterized. But it shows negligible amount of redox reactions and very high impedance values due to poor electrochemical activity of the CVD graphene (Supplementary Fig. 6a–c). On the other hand, the graphene-hybrid electrode shows lower R_{ct} and higher charge storage capacity (CSC) than other electrodes (Fig. 2b,c) due to the increase of electrochemically active surface area by the Au doping with the high thermal and cyclic stability (Supplementary Fig. 5c,d).

Electrochemically active surface areas of electrodes are estimated by using the Randles-Sevcik equation[1] and the well-known diffusion coefficient of ferri- and ferro-cyanide ions in aqueous media[2]. The graphene-hybrid electrode has a larger electrochemically active surface area than other electrodes (i.e., Au mesh and Au film; see Supplementary Table 1). We also calculated the electrochemically active surface area of other 2D[3] and 3D[4,5] graphene electrodes reported in the previous literatures. The results show that the graphene-hybrid electrode has a larger electrochemically active surface area than that of the 2D graphene electrode (calculated value: 0.080), but smaller than those of 3D graphene electrodes (calculated value: 2.189, 4.988). Although 3D graphene electrodes have large surface areas, they are not compatible with several fabrication processes, such as photolithography and transfer printing processes. In addition, they can be irreversibly deformed during wearable device applications, which can cause changes in electrochemical performances of devices. Therefore, our 2D graphene-hybrid electrode is chosen in the current integrated system.

Table 1. CV and AC impedance measurement data and estimated surface area for electrodes

Electrode	R_{ohm} (Ω cm^{-2})	R_{ct} (Ω cm^{-2})	C_{dl} (μF cm^{-2})	CSC (mC cm^{-2})	Normalized Area*
Au film	28	16	21.4534	1.005	0.797
Au mesh	23	490	0.8532	0.252	0.295
Graphene-hybrid	21	15	15.5291	1.307	1.135

*** Normalized Area = Effective Electrochemically Active Surface Area / Geometric Surface Area**

1.2. Mechanical analysis of electrodes.

Finite element modeling (FEM) of the mechanical robustness of the graphene-hybrid electrode is performed using ABAQUS/Standard 6.13. The exploded and cross-sectional views of the multilayer device are illustrated in Supplementary Fig. 8b. Au mesh and graphene sandwiched by epoxy in graphene-hybrid electrode, and Au or ITO film sandwiched by epoxy in conventional electrodes are both modeled as homogeneous shell (mesh element S4R) with different elastic properties. The Young's modulus, Poisson's ratio, and thickness of each layer used in our model are summarized in Supplementary Table 2.

Table 2. Mechanical properties values of different layers[6-10]

Materials	Young's modulus (GPa)	Poisson's ratio	Thickness (nm)
Epoxy	4.02	0.33	1500
Au	79	0.4	70
ITO	116	0.35	150
Graphene	1020	0.15	2
Cr/Au	97	0.39	77

The effective Young's modulus and Poisson's ratio of the Au mesh are calculated by weighing each component's volume fraction[11]. For the graphene-hybrid electrode, we first model an island composed of four blanket layers: epoxy, graphene, Au mesh, epoxy. The effective Young's modulus and Poisson's ratio of the graphene-hybrid electrode is found to be:

$$E_e = 5.0\ GPa, v_e = 0.34.$$

In the following stretching and compression simulation, we model the island and serpentine as a homogeneous shell structure (element type S3) with Young's modulus E_e, Poisson's ratio v_e, and thickness 3079 nm. The substrate (a 0.2 mm thick slab of 1:40 PDMS) is modeled as a 3D Neo Hookean solid (element type C3D10) with coefficients C10 = 6.7 KPa and D1 = 0.003 KPa^{-1}, which corresponds to $E = 40$ KPa and $v = 0.49$[12]. The uniaxial tension experiment with an applied strain of 30 % is simulated by applying symmetric tensile displacements along the top and bottom edges. For the compression simulation, the out of plane displacement at the bottom of the substrate is constrained. We first perform buckling analysis to find four Eigen modes. The Eigen modes are then applied as small perturbation to the perfect geometry. Symmetric compressive displacements are applied at two ends, the postbuckling results can be obtained. The option of nonlinear geometry in ABAQUS has been turned on for both tension and compression to account for large deformation. Figure 21 right shows the maximum principal strain distribution in a local island-serpentine structure. The deformed configurations obtained by FEM match well with the experiment offered in Fig. 2l left. Out-of-plane buckling has been developed in both island and serpentine during compression but just in serpentine during stretching. To compare the mechanical robustness of graphene-hybrid electrode with conventional film electrode mesh, strain distribution in the island after 30 % stretch are presented in Supplementary Fig. 8c. It is clear that graphene-hybrid electrode has relatively smaller strain distribution compared with conventional electrodes. Furthermore, maximum strain as a function of strain is plotted in Fig. 2k, which validates graphene-hybrid electrode experiences lower strains.

1.3. Selective functionalization using the electrodeposition.

Electrodeposition is an efficient technique for the deposition of functional materials on desired active sites without cross-contaminations. We used PEDOT for the humidity sensor, solid-state Ag/AgCl for the counter electrode, PB with the drop-casted GOx for the glucose sensor, and PANi for the pH sensor, along with the Nafion encapsulation. PEDOT is chosen due to its large impedance change to wetting (Supplementary Fig. 12a bottom). The sweat-uptake of Nafion facilitates the increase of the sensitivity (Supplementary Fig. 3a). The solid-state Ag/AgCl counter electrode enables the sensor operation in the two-electrode system. The solid-state Ag/AgCl electrode exhibits similar OCP values versus commercial Ag/AgCl electrode (Supplementary Fig. 12b bottom). PB is chosen to exploit its high catalytic activity to H_2O_2, which is a by-product of the reaction between GOx and glucose (Supplementary Fig. 12c bottom). PANi is chosen due to its changes of surface protonation at different pH values. After electrodeposition of PANi, the electrode shows larger zeta potential changes at different pH values (Supplementary Fig. 12d bottom). This selective functionalization enables the integration of different types of sensors and counter electrodes on one platform.

1.4. Effects of environmental conditions on the glucose sensor operation.

Accuracy and sensitivity of the glucose sensor based on glucose oxidase can be affected by environmental conditions such as i) pH, ii) temperature, iii) common drugs, iv) oxygen level, and v) glucose on the skin.

i) pH effect: The pH dependency of the glucose sensor is estimated at different pH values (Supplementary Fig. 14c), and is used to adjust the glucose concentration to obtain corrected glucose concentration (Figs. 3f and 4f).

ii) Temperature effect: The sensitivity of the glucose sensor is slightly decreased as the temperature decreases, while the sensitivity of the pH sensor is similar at various temperatures (Supplementary Fig. 16a,b). The sensitivity variation of the glucose sensor due to the ambient temperature change can be adjusted by using its pre-calibration data at different temperatures. The ambient temperature can be monitored by the integrated temperature sensor in the diabetes patch.

iii) Interaction with common drugs: The effect of drug interactions on the sensitivity of the glucose sensor is estimated with three commonly used drugs (Tylenol, Aspirin, and Metformin)[13]. We used drug concentrations commonly found in the patient's blood[14,15]. We could selectively measure the glucose concentration without disturbances (Supplementary Fig. 16c). There was a report that Nafion minimized the interference of acetaminophen (Tylenol) in glucose sensing[16]. Our sweat-uptake layer (Nafion) could play a similar role.

iv) Oxygen level effect: Changes of oxygen levels in the blood can affect the sensitivity of glucose sensors based on the glucose oxidase[17-19]. Fluctuations in oxygen concentrations can cause the glucose sensor to underestimate or overestimate glucose levels. However, the glucose oxidase in our glucose sensor is already in contact with the air. The oxygen amount in the air is much larger than that in the blood and/or sweat. The glucose sensor is also calibrated under the air condition. Therefore, the influence on the glucose oxidase would be minimal, although the oxygen concentration in the secreted sweat may be fluctuated. The sweat glucose concentration data measured by our glucose sensor show good linear correlations with those measured by the commercial glucose assay (Supplementary Fig. 17b) and with blood glucose concentration data measured by the commercial glucose meter (Supplementary Fig. 17c).

v) Effect of glucose on the skin: Although there can exist the glucose in the outer layer of skin that is not related with the blood/interstitial fluid/sweat, its amount is not large[20,21] enough to affect the sweat glucose sensing in our diabetes patch. We measured sweat glucose concentrations without considering the glucose in the outer layer of skin and the results showed a good linear correlation with blood glucose concentrations measured by the commercial glucose meter (Supplementary Fig. 17c). The amount of depleted glucose in sweat glucose monitoring process does not disturb the signal read by our diabetes patch. And glucose in stratum corneum[22] which is not related with that in the blood is much lower than sweat glucose levels (0.1~0.7 mM). Therefore, additional warm-up period to ensure the depletion of glucose in the stratum corneum is not needed in our diabetes system.

1.5. Comparison of the glucose sensor with previous reports.

Our glucose sensor performances are compared with previous reports in references[23-28]. Detection limits, sensing ranges, and sensitivity of each sensor are summarized in Table 3. All glucose sensors including ours show high selectivity by virtue of the glucose oxidase. Although our glucose sensor has comparable performances with previous reports, our diabetes patch can systematically correct potential errors in sweat glucose measurements by pH and temperature fluctuations, providing more accurate noninvasive sensing than other technologies. Therefore, reliable and repeatable glucose monitoring was available in our diabetes patch.

Table 3. Comparison of state-of-the-art glucose biosensors[23-28].

Base materials	Substrate	Detection limit (µM)	Sensing range (mM)	Sensitivity (µA mM^{-1})	Ref.
GOx/PB/graphene-hybrid	PDMS	10	0.01-0.7	1.0	This work
GOx/Pt NP/graphene	Glass	0.5	0.05-1	580	23
GOx/graphene	Silk	0.1	0.1-10	2.5	24
GOx/Pt NP/graphene petal	Silicon	0.3	0.01-50	0.65	25
GOx/PB	Tattoo	3	0.003-0.1	23	26
GOx/MWCNT/Pt	Glass	20	0.02-1	5.0	27
GOx/MWCNT	GCE	5	0.005-2.5	2.8	28

1.6. Lag time between blood and sweat glucose level.

It is well-known that there is a time lag between blood glucose levels and sweat glucose levels (~20 minutes)[29]. In our 'point-of-care' monitoring system, the humidity sensor first measures relative humidity (RH) changes inside the diabetes patch and then determines the optimum point to start the measurement of other sensors (e.g., glucose and pH sensors). This minimizes detection errors of point-of-care measurements. To maintain the same situation, we started from the sweat collection in every test. On average, it takes ~15 minutes (10~20 minutes) to gather sweat by the sweat-uptake layer in the patch and glucose/pH sensors start to measure when the RH reaches ~80 % (Fig. 4c). Therefore, the sweat glucose concentration data measured by the diabetes patch and the commercial glucose assay are obtained ~15 minutes after the blood glucose concentration data are measured by the commercial glucose meter.

1.7. Feedback therapy using thermo-responsive microneedles.

Bioresorbable polymer microneedles contain drug inside microneedles. Microneedles are immediately dissolved when exposed to fluids, such as the sweat or interstitial fluids. To control the release time and rate instead of instant dissolution/drug release, therefore, we used the PCM, which is spray-coated on microneedles. PCMs, such as fatty acids or fatty alcohols, are biocompatible and/or bio-inert. The PCM used in this study (tridecanoic acid) is thermo-responsive, passivates microneedles, separates microneedles from moistures below the transition temperature, and melts at temperatures above the body temperature (41–42 °C). The HPLC analysis of Metformin concentration *in-vitro* shows that PCM effectively prevents the release of Metformin under the transition temperature of PCM but allows the drug release above the transition temperature (Fig. 4i and Supplementary Fig. 19b).

Depending on the condition of patients, the amount of drug that needs to be delivered at one time is different. If the patient needs only a small amount of drug at one time, the drug can be delivered in four separate stages as shown in Supplementary Fig. 19d and e. If the patient needs more amount of drug, the amount of drug delivered at one time can be doubled by delivering the drug in two separate stages as shown in Fig. 4j and k. By increasing the total area of microneedles, the maximum number and/or amount of the drug delivery can be increased.

2. References

1) Hrapovic, S., Liu, Y., Male, K. B. & Luong, J. H. T. Electrochemical biosensing platforms using platinum nanoparticles and carbon nanotubes. *Anal. Chem*. **76**, 1083-1088 (2004).

2) Konopka, S. J. & Bruce, M. Diffusion coefficients of ferri- and ferrocyanide ions in aqueous media, using twin-electrode thin-layer electrochemistry. *Anal. Chem*. **42**, 1741-1746 (1970).

3) Anisha, N. P. *et al*. A new view of electrochemistry at highly oriented pyrolytic graphite. *J. Am. Chem. Soc*. **134**, 20117-20130 (2012).

4) Thazhe, V. V., Subbiah, A. & Tharangattu, N. N. The improved electrochemical performance of cross-linked 3D graphene nanoribbon monolith electrodes. *Nanoscale*. **7**, 6504-6509 (2015).

5) Xiaochen, D. *et al*. 3D graphene foam as a monolithic and macroporous carbon electrode for electrochemical sensing. *ACS Appl. Mater. Interfaces*. **4**, 3129-3133 (2012).

6) Guérin, L. J., Bossel, M., Demierre, M., Calmes, S. & Renaud, P. Simple and low cost fabrication of embedded microchannels by using a new thick-film photoplastic. *Proc. Transducers* **2**, 1419-1422 (1997).

7) Williams, J. D. & Wang, W. Using megasonic development of SU-8 to yield ultra-high aspect ratio microstructures with UV lithography. *Microsyst. Technol.* **10**, 694-698 (2004).

8) Kelly, P.F. Properties of Materials. p. 355 (CRC Press, Talyor & Francis Group, 2015).

9) Neerinck, D. G. & Vink, T. J. Depth profiling of thin ITO films by grazing incidence X-ray diffraction. *Thin Solid Films* **278**, 12-17 (1995).

10) Kudin, K. N., Scuseria, G. E. & Yakobson, B. I. C_2F, BN, and C nanoshell elasticity from *ab initio* computations. Phys. Rev. B **64**, 235406 (2001).

11) Wang, A.-J. & McDowell, D. L. In-plane stiffness and yield strength of periodic metal honeycombs. *J. Eng. Mater. Tech.* **126**, 137-156 (2004).

12) Eroshenko, N., Ramachandran, R., Yadavalli, V. K. & Rao, R. R. Effect of substrate stiffness on early human embryonic stem cell differentiation. *J. Biol. Eng*. **7**:7 (2013).

13) Young, D. S., Thomas, D. W., Friedman, R. B. & Pestaner, L. C. *Effects of drugs on clinical laboratory tests*. 4th, **3**, 374-391 (AACC Press, Washington DC, 1995).

14) Tang, Z., Du, X., Louie, F. R. & Kost, J. G. Effects of drugs on glucose measurements with handheld glucose meters and a portable glucose analyzer. *Am. J. Clin. Pathol*. **113**, 75-86 (2000).

15) Hirst, A. J., Farmer, J. A., Ali, R., Roberts, W. N. & Stevens, J. R. Quantifying the effect of metformin treatment and dose on glycemic control. *Diabetes Care*. **35**, 446-454 (2012).

16) Zhang, Y. *et al*. Elimination of the acetaminophen interference in an implantable glucose sensor. *Anal. Chem*. **66**, 1183-1188 (1994).

17) Chun, T.-Y. *et al*. The effect of the partial pressure of oxygen on blood glucose concentration

examined using glucose oxidase with ferricyan ion. *Anesth. Analg.* **79**, 993-997 (1994).

18) Kurahashi, K., Maruta, H., Usuda, Y. & Ohtsuka, M. Influence of blood sample oxygen tension on blood glucose concentration using an enzyme-electrode method. *Crit. Care Med.* **25**, 231-235 (1997).

19) Kost, G. J. *et al.* Multicenter study of oxygen-insensitive handheld glucose point-of-care testing in critical care/hospital/ambulatory patients in the United States and Canada. *Crit. Care Med.* **26**, 581-590 (1998).

20) Kost, J., Mitragotri, S., Gabbay, A. R., Pishko, M & Langer, R. Transdermal monitoring of glucose and other analytes using ultrasound. *Nature Med*. **6**, 347-350 (2000).

21) Xudong, G. *et al*. Detection of trace glucose on the surface of a semipermeable membrane using a fluorescently labeled glucose-binding protein: a promising approach to noninvasive glucose monitoring. *J. Diabetes Sci. Technol*. 7, 4-12 (2013).

22) Takagi, Y., Kriehuber, E., Imokawa, G., Elias, P. M. & Holleran, W. M. β-Glucocerebrosidase activity in mammalian stratum corneum. *J. Lipid Res*. **40**, 861-869 (1999).

23) Zhang, M. *et al.* Highly sensitive glucose sensors based on enzyme-modified whole-graphene solution-gated transistors. *Sci. Rep*. **5**, 8311 (2015).

24) You, X. & Pak, J. J. Graphene-based field effect transistor enzymatic glucose biosensor using silk protein for enzyme immobilization and device substrate. *Sens. Actuators, B* **202**, 1357-1365 (2014).

25) Claussen, J. C. *et al.* Nanostructuring platinum nanoparticles on multilayered graphene petal nanosheets for electrochemical biosensing. *Adv. Funct. Mater.* **22**, 3399-3405 (2012).

26) Bandodkar, A. J. *et al.* Tattoo-based noninvasive glucose monitoring: a proof-of-concept study. *Anal. Chem.* **87**, 394-398 (2015).

27) Tang, H., Yan, F., Lin, P., Xu, J. & Chan, H. L. W. Highly sensitive glucose biosensors based on organic electrochemical transistors using platinum gate electrodes modified with enzyme and nanomaterials. *Adv. Funct. Mater.* **21**, 2264-2272 (2011).

28) Tang, W., Li, L., Wu, L., Gong, J. & Zeng, X. Glucose biosensor based on a glassy carbon electrode modified with polythionine and multiwalled carbon nanotubes. *PLoS ONE* **9**, e95030 (2014).

29) Klonoff, C. D. Noninvasive blood glucose monitoring. Diabetes Care. 20, 433-437 (1997).

DOI: 10.1038/NNANO.2016.38

Supplementary Figures

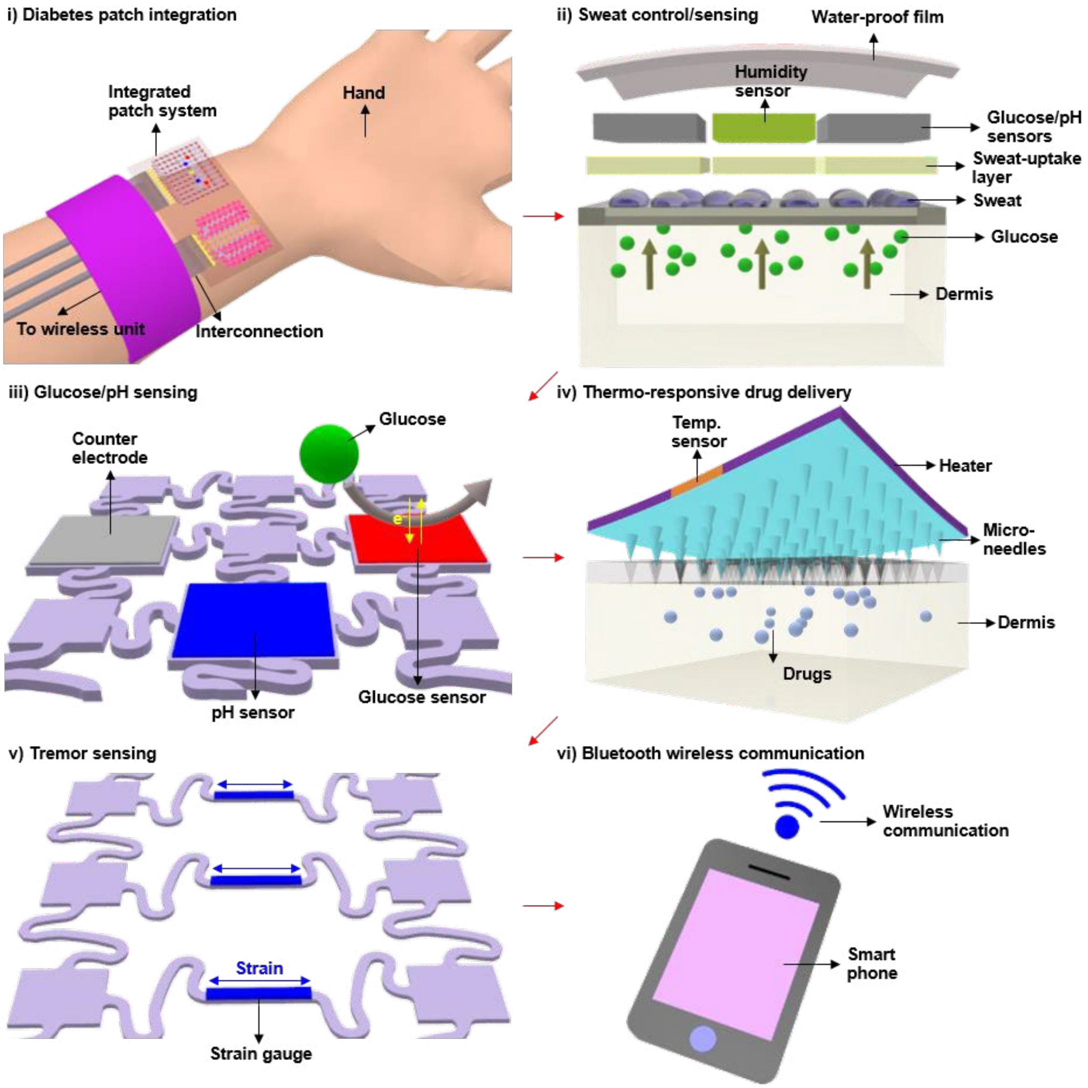

Supplementary Fig. 1. Operation process of the diabetes monitoring and therapy system. Schematic illustrations of the system-level operation. The diabetes patch controls the sweat, in which integrated graphene-hybrid electrochemical sensors monitor markers for diabetes. Thermal actuation through heaters initiates the feedback transdermal drug delivery via thermo-responsive microneedles in the hyperglycaemia. The hypoglycaemia can be detected by the tremor sensor. Monitored data are wirelessly transmitted to remote electronic devices, such as smart phones.

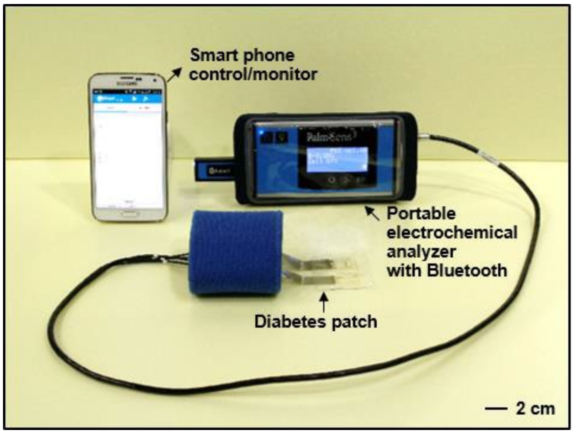

Supplementary Fig. 2. Portable electrochemical analyzer. Graphene-hybrid electrochemical devices are connected to the portable electrochemical analyzer that supplies power to and controls the devices and wirelessly transfers data to remote mobile devices (such as smart phone or tablet computer) via Bluetooth.

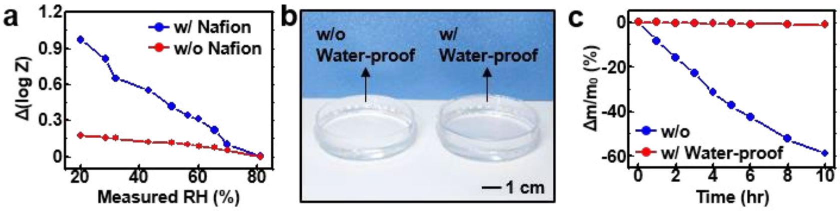

Supplementary Fig. 3. Characterization of the sweat-uptake layer and water-proof film. **a,** Characteristic responses of the humidity sensor with (blue) and without (red) the sweat-uptake layer (Nafion). **b,** Optical camera image of the experimental setup for the water evaporation test. The water-proof film is difficult to see due to its transparency. **c,** Relative mass changes of water by the evaporation with (red) and without (blue) the water-proof film.

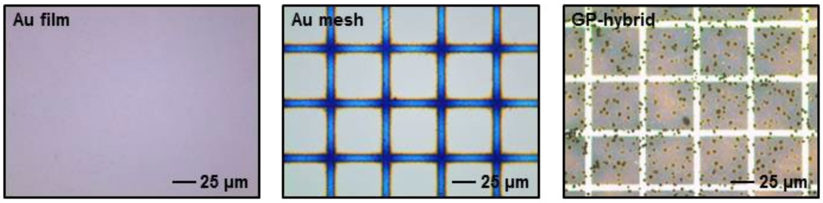

Supplementary Fig. 4. Optical images after the PEDOT electrodeposition. Large scale optical images after the PEDOT electrodeposition on Au film (left), Au mesh (center), and graphene-hybrid electrode (right).

DOI: 10.1038/NNANO.2016.38

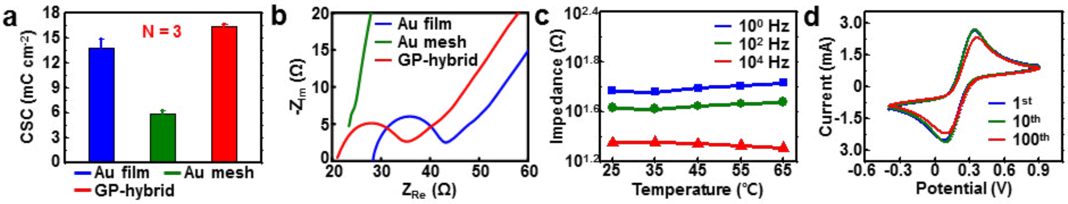

Supplementary Fig. 5. Electrochemical characterization of graphene-hybrid. a, Charge storage capacities of the Au film, Au mesh, and graphene-hybrid electrodes in Fig. 2b (number of samples = 3, error bars show the standard deviation). **b,** Magnified view of Nyquist plots of Au film, Au mesh, and graphene-hybrid electrode in PBS with $Fe(CN)_6^{3-/4-}$ at equilibrium potential. **c,** Electrical stability test of graphene-hybrid electrode at different temperatures and AC frequencies in PBS with $Fe(CN)_6^{3-/4-}$ at equilibrium potential. **d,** Stability test of graphene-hybrid electrode after multiple CV measurements in PBS with $Fe(CN)_6^{3-/4-}$ (scan rate: 0.1 V s^{-1} with the commercial Ag/AgCl electrode).

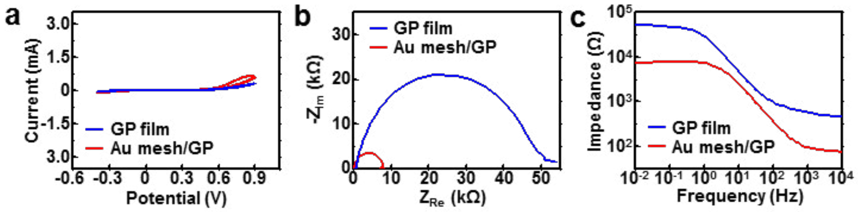

Supplementary Fig. 6. Electrochemical properties of graphene film and Au mesh/graphene. a, CV plots of the graphene film and the Au mesh/graphene in PBS with $Fe(CN)_6^{3-/4-}$ (scan rate: 0.1 V s^{-1} with the commercial Ag/AgCl electrode). **b,** Nyquist plots of the graphene film and Au mesh/graphene in PBS with $Fe(CN)_6^{3-/4-}$ at the same potential with that of Fig. 2c. **c,** Bode plots of graphene film and Au mesh/graphene in PBS with $Fe(CN)_6^{3-/4-}$ at the same potential with that of Fig. 2d.

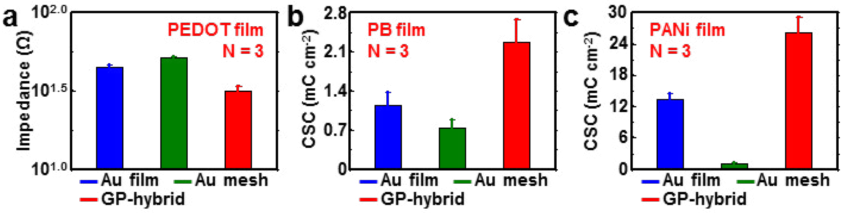

Supplementary Fig. 7. Reproducibility of electrochemical characterization of electrodes (Au film, Au mesh, and graphene-hybrid electrode) after functionalization. a, Impedances of the Au film, Au mesh, and graphene-hybrid electrodes at 100 Hz after electrodeposition of PEDOT under the same condition used in Fig. 2e (number of samples = 3, error bars show the standard deviation). **b,** Charge storage capacities of the Au film, Au mesh, and graphene-hybrid electrodes after electrodeposition of PB under the same condition used in Fig. 2f (number of samples = 3, error bars show the standard deviation). **c,** Charge storage capacities of the Au film, Au mesh, and graphene-hybrid electrodes after electrodeposition of PANi under the same condition used in Fig. 2g (number of samples = 3, error bars show the standard deviation).

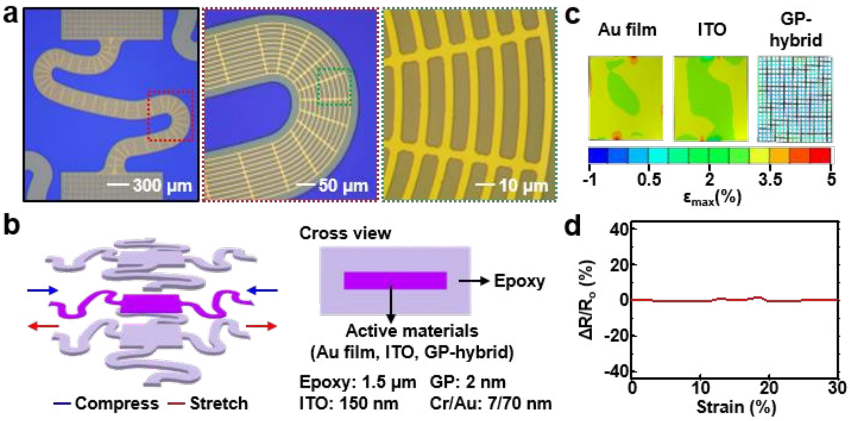

Supplementary Fig. 8. Design strategy and mechanical simulation for the graphene-hybrid electrode. a, Optical microscope images of the Au mesh and graphene bilayer electrode. Serpentine-shaped Au mesh boosts up both the conductivity and mechanical deformability. **b,** Layer information of the graphene-hybrid and conventional electrode. **c,** Strain distribution analysis in the island of Au film, ITO, and graphene-hybrid electrode after 30 % stretching. **d,** Relative resistance change of the graphene-hybrid electrode under applied strains up to ~30 %.

DOI: 10.1038/NNANO.2016.38

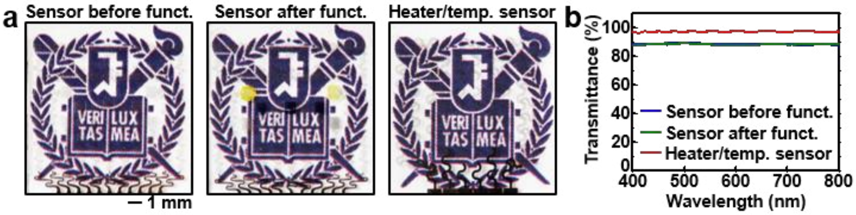

Supplementary Fig. 9. Transparency of the array of graphene-hybrid electrochemical sensors and the heater/temperature sensor. a, Optical camera images of the sensor array before (left) and after (center) functionalization on the university logo. Right frame shows the heater/temperature sensor array on the university logo. The logo can be clearly seen through devices due to the transparency. **b,** Corresponding transmittance data of each sample.

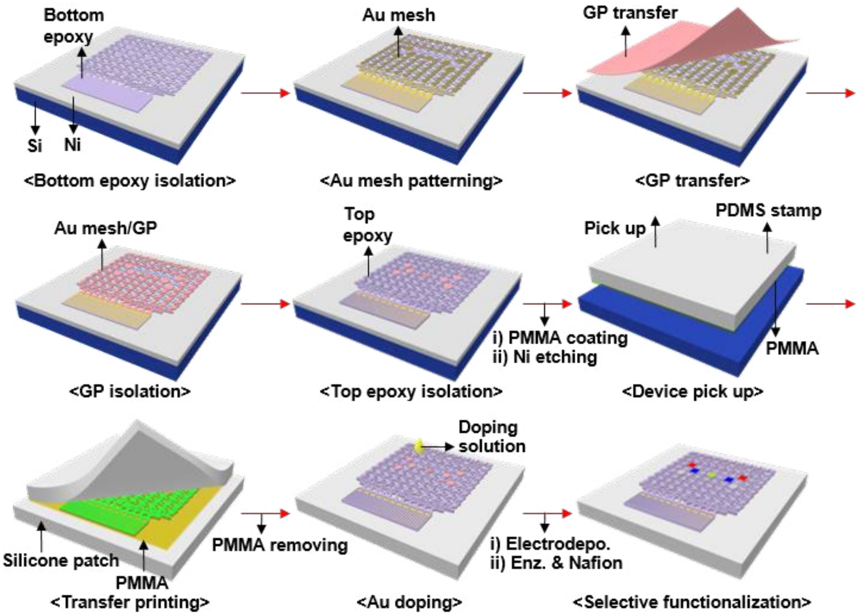

Supplementary Fig. 10. Device fabrication process. Schematic illustration of the fabrication process of the graphene-hybrid electrochemical sensor array.

DOI: 10.1038/NNANO.2016.38

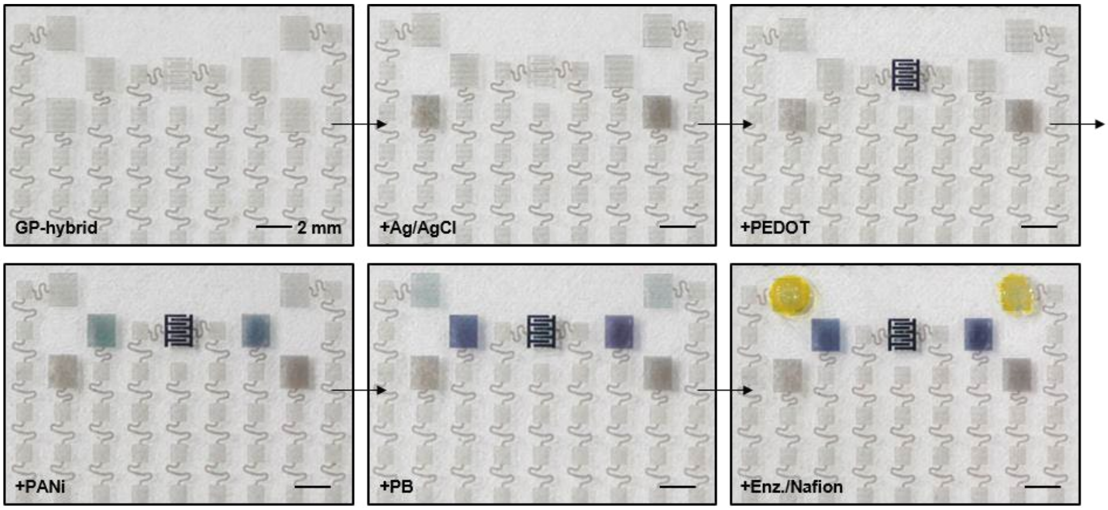

Supplementary Fig. 11. Selective functionalization process of the graphene-hybrid sensors and Ag/AgCl solid-state counter electrode. Optical camera images of the step-wise selective functionalization process of graphene-hybrid. No cross-contaminations are observed.

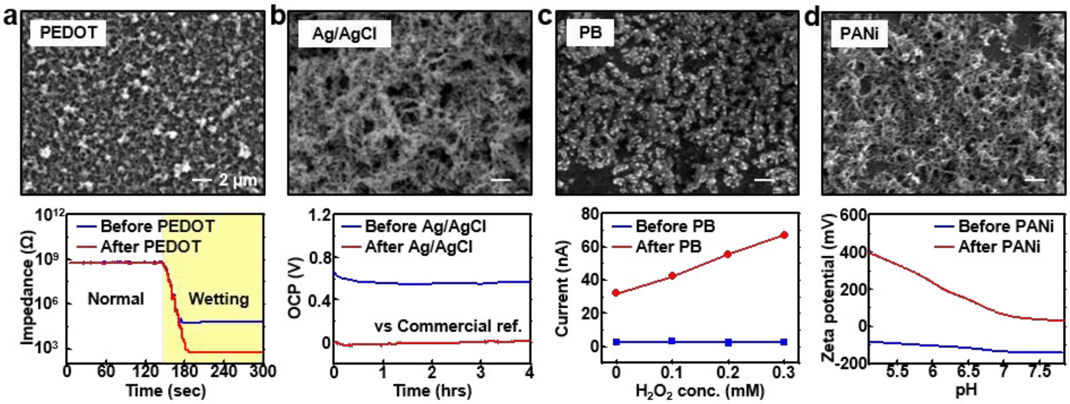

Supplementary Fig. 12. Characterization of functionalized materials of the graphene-hybrid. a, PEDOT electrodeposition on the graphene-hybrid electrode (doped graphene and Au mesh bilayer) for the humidity sensor (top: SEM image, bottom: impedance changes by wetting before and after the PEDOT deposition). **b,** Ag/AgCl electrodeposition for the counter electrode (top: SEM image, bottom: OCP changes before and after Ag/AgCl deposition vs. commercial Ag/AgCl electrode). **c,** PB electrodeposition for the glucose sensor (top: SEM image, bottom: H_2O_2 sensitivity comparison before and after the PB deposition at different H_2O_2 concentrations, initial potential: -0.05 V vs. commercial Ag/AgCl electrode). **d,** PANi electrodeposition for the pH sensor (top: SEM image, bottom: zeta potential changes before and after the PANi deposition).

DOI: 10.1038/NNANO.2016.38

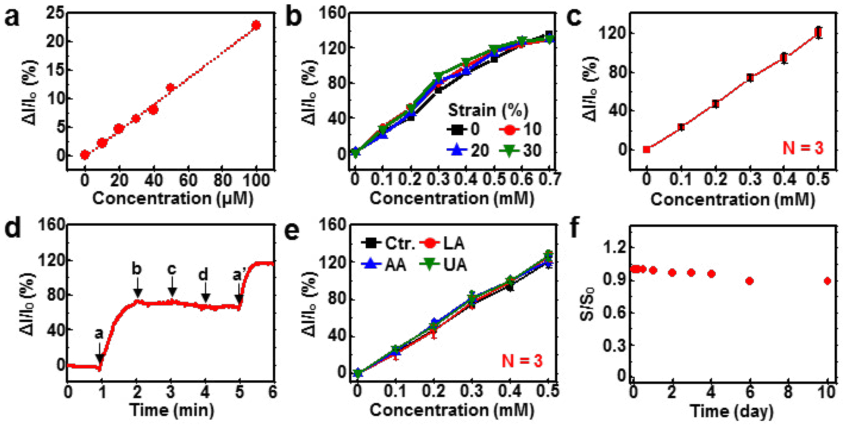

Supplementary Fig. 13. Characterization of glucose sensor. a, Calibration curves of the glucose sensor at low glucose concentrations (initial potential: -0.05 V vs. solid-state Ag/AgCl electrode). **b,** Calibration curves of the glucose sensor at different applied strains (initial potential: -0.05 V vs. solid-state Ag/AgCl electrode). **c,** Reproducible operation of the glucose sensor (number of samples = 3, error bars show the standard deviation, initial potential: -0.05 V vs. solid-state Ag/AgCl electrode). **d,** Selectivity of the glucose sensor (a: 0.3 mM glucose, b: 4 mM lactate, c: 10 μM ascorbic acid, d: 59 μM uric acid, a′: 0.5 mM glucose, initial potential: -0.05 V vs. solid-state Ag/AgCl electrode). Glucose sensor responds to glucose concentration changes only. **e,** Selective operation of the glucose sensor (black: glucose only, red: glucose with 4 mM lactate, blue: glucose with 10 μM ascorbic acid, green: glucose with 59 μM uric acid, number of samples = 3, error bars show the standard deviation, initial potential: -0.05 V vs. solid-state Ag/AgCl electrode). **f,** Long-term stability of the glucose sensor (initial potential: -0.05 V vs. solid-state Ag/AgCl electrode).

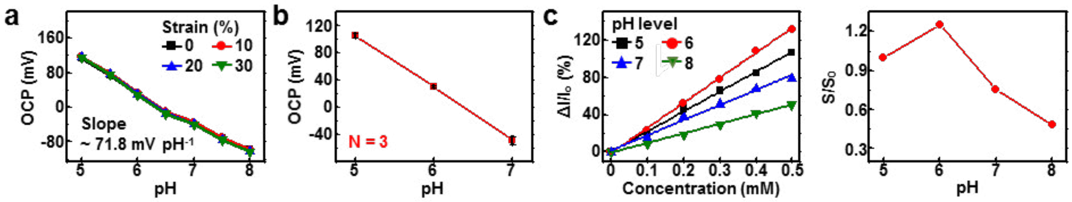

Supplementary Fig. 14. Characterization of pH sensor and pH dependency of glucose sensor. a, pH-dependent OCP changes of the pH sensor at different applied strains (OCP vs. solid-state Ag/AgCl electrode). **b,** Reproducible operation of the pH sensor (number of samples = 3, error bars show the standard deviation, OCP vs. solid-state Ag/AgCl electrode). **c,** pH dependency of the glucose sensor (left: relative current changes of the glucose sensor at different pH, right: relative sensitivity changes of glucose sensor at different pH, initial potential: -0.05 V vs. solid-state Ag/AgCl electrode).

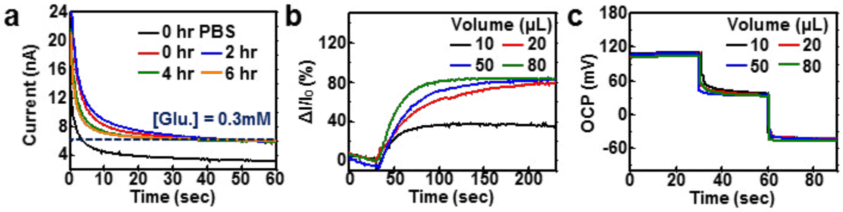

Supplementary Fig. 15. Stability of glucose sensor and influence of sweat amount test on glucose and pH sensors. a, Stability test of the glucose sensor for 6 hours using the artificial sweat (0.3 mM, initial potential: -0.05 V vs. solid-state Ag/AgCl electrode). **b,** Influence of sweat amount (or relative humidity) on the glucose sensor (initial potential: -0.05 V vs. solid-state Ag/AgCl electrode). **c,** Influence of sweat amount (or relative humidity) on the pH sensor (OCP vs. commercial Ag/AgCl electrode).

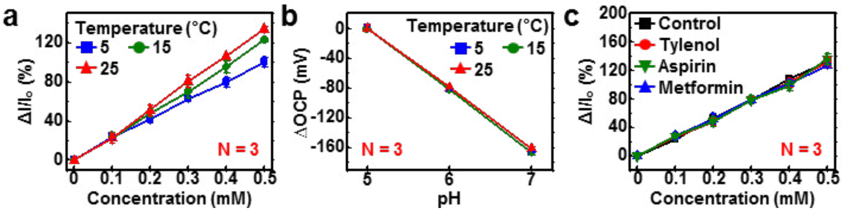

Supplementary Fig. 16. Temperature dependency of glucose/pH sensors and drug interaction test of the glucose sensor. a, Calibration curves of the glucose sensor at different temperatures (number of samples = 3, error bars show the standard deviation, initial potential: -0.05 V vs. solid-state Ag/AgCl electrode). **b,** Open circuit potential changes of the pH sensor at different temperatures (number of samples = 3, error bars show the standard deviation, OCP vs. commercial Ag/AgCl electrode). **c,** Calibration curves of the glucose sensor in a series of test solutions (black: glucose only, red: glucose with 20 µg mL^{-1} Tylenol, green: glucose with 100 µg mL^{-1} Aspirin, blue: glucose with 100 µg mL^{-1} Metformin, number of samples = 3, error bars show the standard deviation, initial potential: -0.05 V vs. solid-state Ag/AgCl electrode).

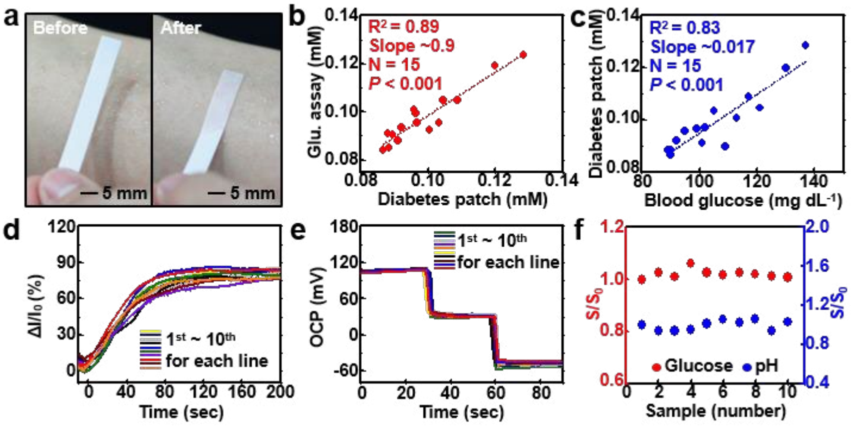

Supplementary Fig. 17. Sweat generation, statistical correlation, and multiple reuses. a, Optical camera images of the generated sweat, checked by the cobalt chloride paper. **b,** Statistical analysis of the correlation between the sweat glucose concentration measured by the diabetes patch and that measured by the commercial glucose assay. Small *P* value shows that the results are statistically reliable ($P < 0.001$). **c,** Statistical analysis of the correlation between the sweat glucose concentration measured by the diabetes patch and the blood glucose concentration measured by the commercial glucose meter. Small *P* value shows that the results are statistically reliable ($P < 0.001$). **d,** Stable operation of the glucose sensor after multiple reuses (initial potential: -0.05 V vs. solid-state Ag/AgCl electrode) using the artificial sweat (0.3 mM). **e,** Stable operation of the pH sensor after multiple reuses (OCP vs. solid-state Ag/AgCl electrode) using standard pH buffer solutions (pH 5, 6, 7). **f.** Plots showing the stable sensitivity of glucose and pH sensor in multiple sensors.

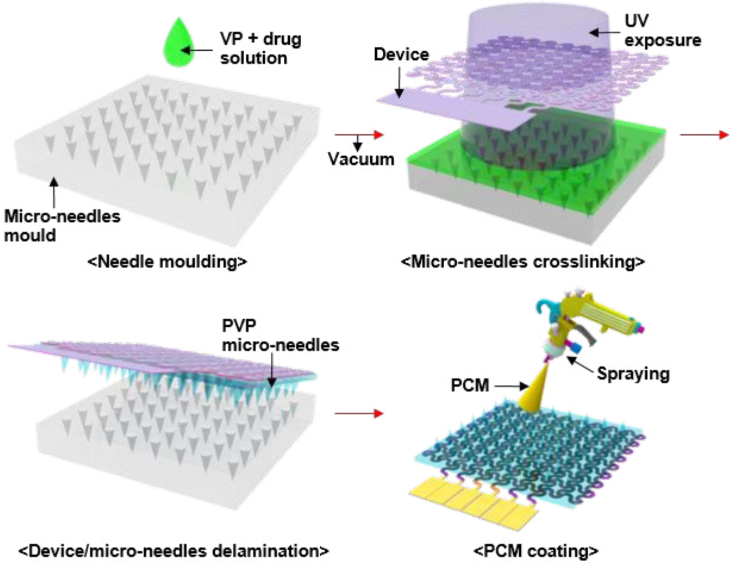

Supplementary Fig. 18. Fabrication process of the drug-loaded microneedles. Schematic illustrations of the fabrication process of the drug-loaded microneedles. Microneedles are made of the bioresorbable polymer (PVP) and coated with the biocompatible PCM (tridecanoic acid).

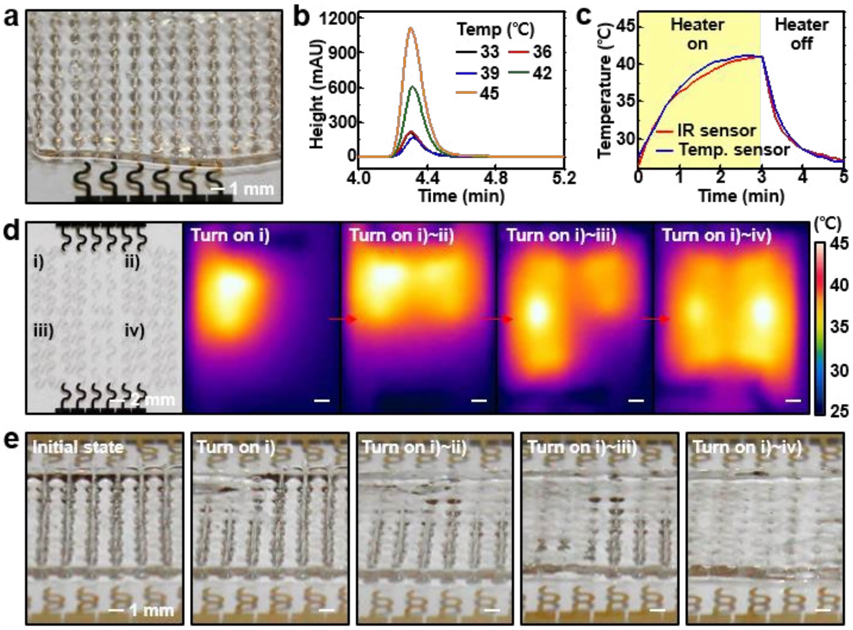

Supplementary Fig. 19. Characterization of microneedles, embedded heaters, and a temperature sensor. a, Optical camera image of microneedles integrated on the array of heaters and a temperature sensor. **b,** HPLC analysis data of drug concentrations during the thermo-responsive drug release of Fig. 4i. **c,** Temperature monitoring of the heater by using a commercial infrared camera and the integrated temperature sensor. **d,** Step-wise thermal actuation of microneedles by using the 4 channel heater array. This enables the multi-step drug release. **e,** Optical camera images of the step-wise dissolution of microneedles corresponding to the thermal actuation in Supplementary Fig. 19d.

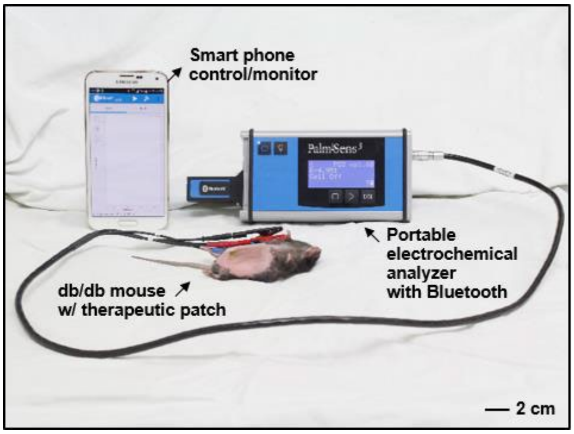

Supplementary Fig. 20. *In vivo* animal experiment setup for the transdermal drug delivery using thermo-responsive microneedles. Image of the *in vivo* experimental setup for the integrated therapeutic system (drug-loaded microneedles, heater, and a temperature sensor) connected to the portable electrochemical analyzer.

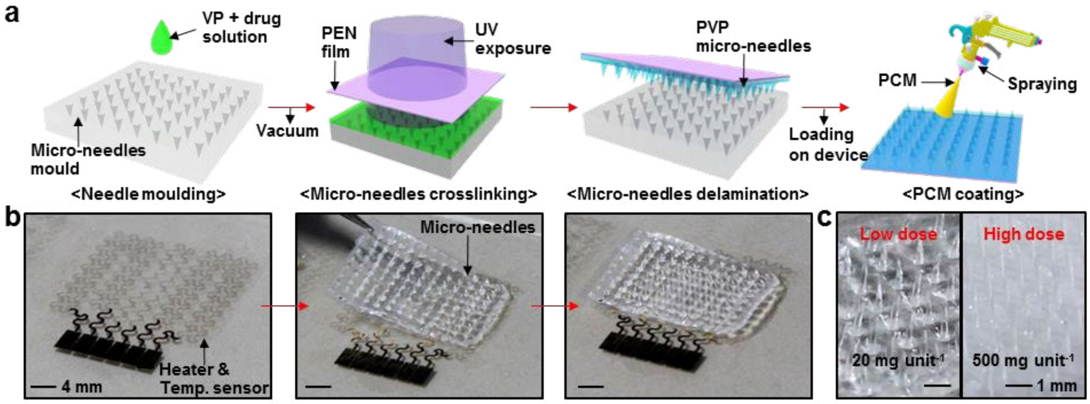

Supplementary Fig. 21. Fabrication process and images of the replacement type microneedles. a, Schematic illustrations of the fabrication process of the drug-loaded microneedles. **b,** Optical image of replacement type microneedles on the heater and temperature sensor (left: before transfer, middle: during transfer, right: after transfer). **c,** Optical images of replacement type microneedles with different amount of loaded Metformin (left: low dose; ~20 mg unit^{-1}, right: high dose; ~500 mg unit^{-1}).